OPEN ACCESS
IOP Publishing | International Atomic Energy Agency
Nuclear Fusion
Nucl. Fusion **65** (2025) 016062 (26pp)
https://doi.org/10.1088/1741-4326/ad9ab9

# Influence of the density gradient on turbulent heat transport at ion-scales: an inter-machine study with the gyrokinetic code `stella`

**H. Thienpondt[1,*], J.M. García-Regaña[1], I. Calvo[1], G. Acton[2] and M. Barnes[2]**

[1] Laboratorio Nacional de Fusión, CIEMAT, 28040 Madrid, Spain
[2] Rudolf Peierls Centre for Theoretical Physics, University of Oxford, Oxford OX1 3NP, United Kingdom of Great Britain and Northern Ireland

E-mail: Hanne.Thienpondt@ciemat.es

Received 16 April 2024, revised 26 November 2024
Accepted for publication 5 December 2024
Published 17 December 2024

**Abstract**

Efficient control of turbulent heat transport is crucial for magnetic confinement fusion reactors. This work discusses the complex interplay between density gradients and microinstabilities, shedding light on their impact on turbulent heat transport in different fusion devices. In particular, the influence of density gradients on turbulent heat transport is investigated through an extensive inter-machine study, including various stellarators such as W7-X, LHD, TJ-II and NCSX, along with the Asdex Upgrade tokamak (AUG) and the tokamak geometry of the Cyclone Base Case (CBC). Linear and nonlinear simulations are performed employing the $\delta f$-gyrokinetic code `stella` across a wide range of parameters to explore the effects of density gradients, temperature gradients, and kinetic electrons. A strong reduction in ion heat flux with increasing density gradients is found in NCSX and W7-X due to the stabilization of temperature-gradient-driven modes without significantly destabilizing density-gradient-driven modes. In contrast, the tokamaks exhibit an increase in ion heat flux with density gradients. Notably, the behavior of ion heat fluxes in stellarators does not align with that of linear growth rates, if only the fastest-growing mode is taken into account. Additionally, this study provides physical insights into the microinstabilities, emphasizing the dominance of trapped-electron-modes (TEMs) in CBC, AUG, TJ-II, LHD and NCSX, while both the TEM and the passing-particle-driven universal instability contribute significantly in W7-X.

Keywords: gyrokinetics, turbulence, heat transport, stellarators, tokamaks

(Some figures may appear in colour only in the online journal)

* Author to whom any correspondence should be addressed.

## 1. Introduction

To achieve net energy in magnetic confinement fusion reactors, it is important to understand, predict and to some extent control heat transport, and in particular transport caused by turbulence. Experimental observations in both tokamaks [1–6] and stellarators [7–10] indicate that peaked density profiles result in a reduction of turbulent heat transport. This reduction is believed to be related to the stabilization of the ion-temperature-gradient (ITG) and electron-temperature-gradient (ETG) driven modes by large density gradients. However, an increasing density gradient eventually destabilizes density-gradient-driven modes such as trapped-electron-modes (TEM). Hence, the question arises whether there exists a specific range of density gradients wherein temperature-gradient-driven modes are stabilized, without significantly destabilizing the density-gradient-driven modes.

In tokamaks, TEMs are particularly problematic because the majority of the trapped electrons are located in the bad curvature region on the low field side of the device. To explain the observed high-confinement phases in pellet-enhanced performance (PEP) discharges, it is not sufficient to consider density peaking alone. Additional mechanisms that can mitigate turbulence must also be taken into account, such as $E \times B$ shearing, reversed magnetic shear due to large bootstrap current, and high-collisionality which can detrap electrons [11–15]. In contrast, in stellarators, the bulk of trapped electrons may be separated from the bad curvature regions, which reduces the impact of TEMs. Additionally, configurations approaching the maximum-$J$ property have been shown to have reduced TEM turbulence [16–19]. As a result, the classical electron-driven TEM may be significantly less detrimental in stellarators, with other instabilities driven by density gradients, such as ion-driven TEMs (iTEM) and universal instabilities, playing a more prominent role. Moreover, turbulence in stellarators has been shown to be reduced by ambipolar electric fields [20, 21], $E \times B$ shearing, zonal flow shearing, energy cascades to dissipative scales [22–25] and energy transfer through damped modes [26, 27].

In this work, the effect of the density gradient on turbulent heat transport is isolated to explore how density peaking influences turbulent heat transport and how this impact varies across different magnetic configurations. The $\delta f$-gyrokinetic code `stella` [28] is used to carry out a comprehensive comparative study of different devices, including different families of stellarators, specifically, the Wendelstein 7-X (W7-X) stellarator, the Large Helical Device (LHD), the TJ-II stellarator and the National Compact Stellarator Experiment (NCSX), which represent helias, heliotron, heliac and quasi-axisymmetric configurations, respectively. Additionally, the Axially Symmetric Divertor Experiment or ASDEX Upgrade (AUG) tokamak and the tokamak geometry of the Cyclone Base Case (CBC) [29] are included for comparison.

Previous cross-device comparisons of the effect of the density gradient were limited to linear results [30, 31], or only consider a few points in parameter space for nonlinear simulations [17–20, 23, 25, 27]. Specifically, it has been shown that W7-X benefits from reduced ITG turbulence and low TEM-driven transport in the presence of a density gradient [18, 19], however, the influence of the electron temperature gradient was neglected in [18]. On the other hand, the heat transport has been investigated before and after the injection of cryogenic hydrogen pellets in a W7-X discharge, where it is argued that a decrease of turbulence in the presence of peaked density profiles is either due to a transition from ITG to iTEM-driven turbulence [20], or due to a more efficient zonal-flow stabilization in the post-pellet phase [25]. In contrast to previous studies, this work includes both linear and nonlinear results across a broad range of parameters, examining the impact of electrons with and without a temperature gradient, as well as analyzing the velocity dependence of the turbulent component of the distribution function, to investigate the impact of density peaking on turbulence.

The paper is divided into the following sections. First, the simulation domain and the coordinates employed by the gyrokinetic code `stella` are explained in section 2. Next, section 3 introduces and analyzes the different magnetic configurations, and in section 4 the localization of the microinstabilities is inferred from the regions of bad curvature and magnetic wells. In section 5 a comprehensive linear stability analysis of the six considered devices is carried out. The growth rates and frequencies of the microinstabilities are discussed in section 5.1, for specific values of the profile gradients and considering a wide range of radial and binormal wavenumbers. Section 5.2 explores the evolution of the instabilities with increasing density gradients, revealing that the most unstable mode transitions continuously from an ITG driven mode to a predominantly density-gradient-driven mode in CBC, AUG, TJ-II and LHD. In contrast, NCSX and W7-X display distinct frequency branches, indicating that different microinstabilities can be distinguished from one another. In section 5.3 the most unstable mode for the considered binormal wavenumbers is identified, showing that the linear growth rates of the fastest-growing modes increase with the density gradient in CBC, AUG, TJ-II and LHD—and to a lesser extent in NCSX—whereas a modest reduction of the growth rates is found for a small range of density gradients in W7-X. The contributions of the specific plasma gradients are isolated in section 5.4, which reveals that in NCSX and W7-X there is a range of density gradients for which the ITG-driven modes are stabilized, without driving the density-gradient-driven modes particularly unstable yet. To conclude the linear analysis, in section 5.5 the ion temperature and density gradient are scanned across a wide range of parameters.

Section 6 is the most important part of this paper, as it investigates the effect of the density gradient on the turbulent heat transport by means of nonlinear gyrokinetic simulations. Section 6.1 highlights the distinct behaviors of the ion heat flux in different devices. Specifically, in the tokamaks, the ion heat flux increases strongly with the density gradient, whereas in LHD it remains largely unaffected, and in TJ-II a substantial reduction of the ion heat flux occurs

for small density gradients. In contrast, both NCSX and W7-X exhibit a strong reduction of the ion heat flux across a wide range of density gradients, due to the stabilization of temperature-gradient-driven modes, without significantly destabilizing density-gradient-driven modes, as demonstrated in section 6.2. The influence of a finite electron temperature gradient is discussed in section 6.3. It is worth noting that in stellarators the ion heat flux shows no correlation with the growth rates of the fastest-growing modes obtained from the linear analysis. Finally, the distribution function is examined in detail in section 6.4 to characterize the microinstabilities that are driving the turbulence, by means of novel diagnostics developed in `stella`. Specifically, the velocity dependence of the perturbed distribution function is examined to quantify the importance of the ion and electron dynamics, and to determine whether the turbulence is primarily driven by the trapped or passing electrons. It is found that at high density gradients, TEMs predominately drive the heat transport in CBC, AUG, TJ-II, LHD and NCSX, whereas in W7-X, the passing-particle-driven universal instability contributes significantly to the turbulence.

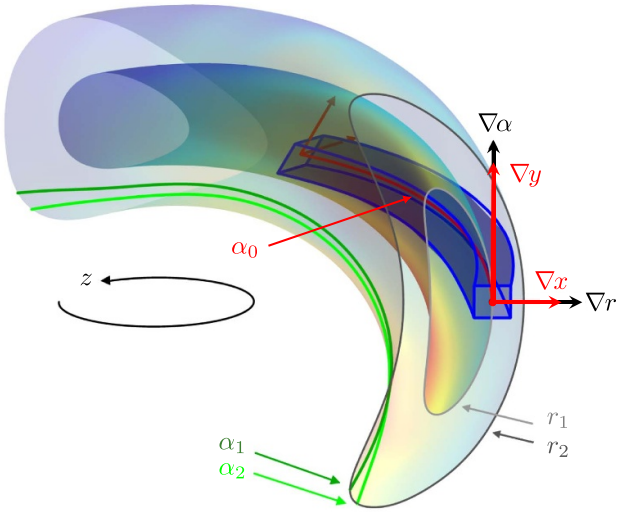


**Figure 1.** Half a period of the Wendelstein 7-X stellarator depicting the coordinates used in `stella`. The last closed flux surface and the flux surface located at $r/a = 0.5$ are shown, highlighting two field lines in green. The flux tube surrounding the $\alpha_0 = 0$ field line (passing through $\theta = 0$ and $\zeta = 0$) at $r/a = 0.5$ is shown in blue, extending a quarter of a period.

## 2. Gyrokinetic code `stella` and coordinates

The flux-tube $\delta f$-gyrokinetic code `stella` [28] is employed, which has been extensively benchmarked for W7-X geometry [32]. Moreover, `stella` has been applied to the study of turbulent particle fluxes [33, 34] and turbulent impurity transport [35–37]. The code evolves electrostatic fluctuations by solving the nonlinear Vlasov and quasi-neutrality equations in five-dimensional phase space. We refer the reader to [28, 32] for a detailed overview of the equations solved by `stella` and to [32] for the explanation of the notation and conventions that we follow here. The magnetic field is written in Clebsch form [38] as $\mathbf{B} = (\mathrm{d}\psi_\mathrm{t}/\mathrm{d}r)\,\boldsymbol{\nabla} r \times \boldsymbol{\nabla}\,\alpha$, with $r = a\sqrt{\psi_\mathrm{t}/\psi_\mathrm{t,LCFS}}$ a flux surface label, which is taken to be the effective minor radius coordinate (gray contours in figure 1), and $\alpha = \theta - \iota\zeta$ a field line label (green lines in figure 1). Here $\psi_\mathrm{t}$ is the toroidal flux divided by $2\pi$, $\psi_\mathrm{t,LCFS}$ is the value of $\psi_\mathrm{t}$ at the last closed flux surface, $a$ is the minor radius, $\iota(r)$ is the rotational transform, and $(\zeta, \theta)$ are straight-field line coordinates, which are chosen to be the cylindrical toroidal angle $\zeta$ and the poloidal PEST coordinate $\theta$ [39]. The simulation domain is restricted to a flux tube (blue box in figure 1), surrounding a chosen magnetic field line $\alpha_0$ (red curve in figure 1). Since $(r, \alpha)$ are field-aligned coordinates, the cross-section of the flux tube is twisted into a parallelogram by the local magnetic shear as one moves along the field line. Note that the cross-section is taken to be rectangular at the center of the flux tube.

The phase-space coordinates employed by `stella` are denoted by $\{x, y, z, v_\parallel, \mu\}$, with $\{x, y, z\}$ a left-handed coordinate system. The local coordinates perpendicular to the magnetic field lines are defined as $x = r - r_0$ and $y = r_0(\alpha - \alpha_0)$. The index '0' refers to quantities that are evaluated on the chosen magnetic field line. The parallel coordinate $z$ measures distances along the field line, hence $\theta$ or $\zeta$ can be used, and it is normalized to $[-\pi, \pi]$. The velocity coordinates consist of the parallel velocity $v_\parallel$ and the magnetic moment $\mu = v_\perp^2/2B$, with $v_\perp$ the perpendicular velocity and $B$ the magnetic field strength. The turbulent distribution function $g_s$ and the perturbed electrostatic potential $\varphi$ are Fourier transformed with respect to the perpendicular $(x, y)$-coordinates. The dimensions $(L_x, L_y)$ of the flux-tube cross-section define the wavenumbers that are included in the simulations, i.e. $k_x = 2\pi m/L_x$ and $k_y = 2\pi n/L_y$, where $m \in \mathbb{Z}$ and $n \in \mathbb{Z}$ are integers. Note that negative $k_y$ values are omitted as they can be recovered using the reality condition $\hat{\varphi}(k_x, k_y, z) = \hat{\varphi}^*(-k_x, -k_y, z)$, with $\hat{\varphi}^*_{\mathbf{k}}$ the complex conjugate of $\hat{\varphi}_{\mathbf{k}}$, and the hat denotes the Fourier coefficients of $\varphi$.

The perpendicular coordinates are normalized with respect to the gyroradius (or Larmor radius) $\rho_\mathrm{i} = v_\mathrm{th,i}/\Omega_\mathrm{i}$ of the ion species, which are taken to be hydrogen nuclei in this work. Here $v_\mathrm{th,i} = \sqrt{2T_\mathrm{i}/m_\mathrm{i}}$ is the reference thermal velocity, $\Omega_\mathrm{i} = eB_\mathrm{ref}/m_\mathrm{i}$ is the reference gyrofrequency, $B_\mathrm{ref} = 2\,|\psi_\mathrm{t,LCFS}|/a^2$ is the reference magnetic field, $T_\mathrm{i}$ is the temperature and $m_\mathrm{i}$ is the mass of the hydrogen nuclei. The parallel coordinate is normalized with respect to the minor radius $a$ and the velocities are normalized with respect to the reference thermal velocity $v_\mathrm{th,i}$. The simulations presented in this paper are electrostatic, collisionless, consider ion-Larmor scales and include both kinetic hydrogen nuclei and electrons, with equal densities $(n_\mathrm{i} = n_\mathrm{e})$ and temperatures $(T_\mathrm{i} = T_\mathrm{e})$. Moreover, the ion and electron density gradients are assumed to be equal $(a/L_{n_\mathrm{i}} = a/L_{n_\mathrm{e}})$ with $a/L_{n_s} = -(a/n_s)\,\mathrm{d}n_s/\mathrm{d}r$ the normalized density gradient.

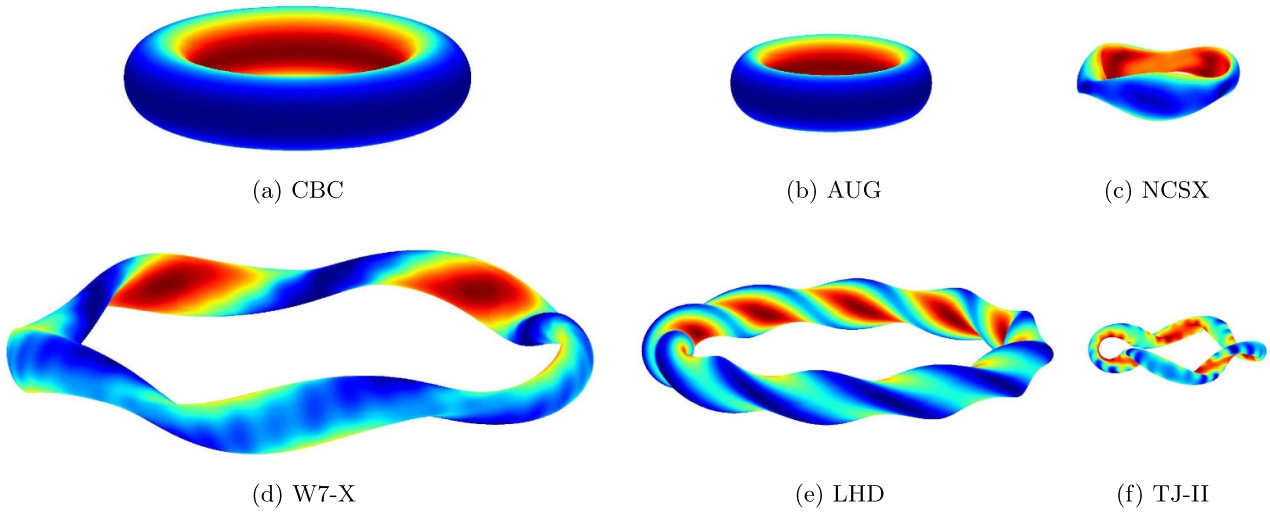


**Figure 2.** Magnetic field strength—minimum is blue, maximum is red—on the flux surface $r/a = 0.7$ for the six considered devices. The same scale is used in order to compare the relative size of the reactors.

## 3. Magnetic configurations

To address the effect of the magnetic geometry on linear growth rates and nonlinear heat transport, this study incorporates the tokamak geometry of the CBC, which has been used extensively to benchmark gyrokinetic codes [29], as well as the AUG tokamak, constructed at IPP (Germany), which commenced operations in 1991. On the other hand, the W7-X, TJ-II, LHD and NCSX stellarators are included. Wendelstein 7-X is a low-shear five-field-period helias configuration, that has been in operation at IPP (Germany) since 2015, for which the standard EIM configuration [40] is used. Another low-shear device is the four-field-period heliac configuration TJ-II, which has been in operation since 1997 at CIEMAT (Spain). The standard configuration (100_44_64) is considered. NIFS (Japan) houses the LHD, a ten-field-period heliotron configuration, generating plasmas since 1998, for which the standard configuration with a major radius of $R_0 = 3.73$ is used. Lastly, NCSX is a three-field-period quasi-symmetric stellarator, in particular featuring toroidal quasi-symmetry, also known as quasi-axisymmetry, developed at PPPL (United States). The magnetic configurations of AUG, TJ-II, LHD, NCSX and W7-X are generated by the three-dimensional MHD equilibium code `VMEC` [41], whereas the considered flux surface of CBC is defined by a set of Miller parameters [42], explicitly given in [28]. The configurations are taken to have $\beta = 0$, with $\beta$ the ratio of the plasma pressure to the magnetic pressure.

In this work, a fixed ion temperature gradient of $a/L_{T_\mathrm{i}} = 3.0$ is considered, while exploring both vanishing ($a/L_{T_\mathrm{e}} = 0.0$) and finite ($a/L_{T_\mathrm{e}} = 3.0$) electron temperature gradients. The density gradient is varied across a broad range of parameters, ranging from $a/L_n = 0.0$ to $a/L_n = 4.0$. These parameters were chosen with the high-performance pellet-injection discharges of W7-X in mind, which are characterized by ($a/L_n = 0.8$ and $a/L_{T_\mathrm{i}} = 2.5$) in the pre-pellet phase and ($a/L_n = 3.0$ and $a/L_{T_\mathrm{i}} = 4.5$) in the post-pellet phase at $r/a = 0.63$ [20, 25]. Given that each device operates under different conditions, the considered gradients may be somewhat extreme for LHD and TJ-II. Nonetheless, examining the impact of density peaking in these devices under such gradients is valuable, as they represent distinct stellarator designs and they provide a clear contrast with the results from the tokamak configurations. It is important to note that this paper focuses on investigating the effects of density peaking on turbulent transport across different reactor designs, rather than on direct comparisons with experimental data.

The simulations are performed at the radial location $r/a = 0.7$, for which the flux surfaces are shown in figure 2. The magnetic field strength is minimum (blue) on the outboard side and maximum (red) on the inboard side of the tokamaks. This trend does not necessarily hold in stellarators, where a minimum of the magnetic field can also be found on the inboard side, and vice versa. An overview of the geometric characteristics of these flux surfaces is given in table 1. For tokamaks, the strongest turbulence is expected to be found at the outboard midplane, therefore gyrokinetic studies generally focus on the $\alpha_0 = 0$ field line centered at $(\theta, \zeta) = (0, 0)$, which lays on the bean-shaped cross-section of W7-X (see figure 1), and the outboard midplane of the tokamaks. Note that the magnetic geometry and plasma parameters included in the simulations depend solely on their values and radial derivatives along the selected magnetic field line $\alpha_0$. Seeing that each field line in a stellarator has a unique magnetic geometry, different field lines will simulate different levels of turbulence [32, 43]. Although in stellarators the turbulence may be strongest elsewhere on the flux surface, this study is limited to the $\alpha_0 = 0$ field line, since it is stellarator-symmetric [44], allowing us to utilize the generalized twist-and-shift boundary conditions [45], which are particularly advantageous for low-shear devices such as TJ-II and W7-X. The flux tube is extended up to three poloidal turns for linear simulations, and up to approximately one poloidal turn for nonlinear

**Table 1.** Geometric quantities at $r/a = 0.7$, with $a$ the minor radius, $R_0$ the major radius, $\hat{s} = (r/q)(\mathrm{d}q/\mathrm{d}r)$ the shear, $\iota = 1/q$ the rotational transform and $q$ the safety factor. $N_\mathrm{f}$ is the number of field periods of the device and $N_\mathrm{pol}$ is the length of the flux tube, given in number of poloidal turns, considered in the nonlinear simulations performed in section 6.

| Device | $a$ (m) | $R_0$ (m) | $\hat{s}$ | $\iota$ | $N_\mathrm{f}$ | $N_\mathrm{pol}$ |
|---|---|---|---|---|---|---|
| CBC | 1.00 | 2.78 | 0.796 | 0.714 | 1 | 1.00 |
| AUG | 0.63 | 1.62 | 1.587 | 0.744 | 1 | 1.00 |
| NCSX | 0.32 | 1.44 | −0.703 | 0.541 | 3 | 0.95 |
| TJ-II | 0.19 | 1.50 | −0.057 | −1.592 | 4 | 1.19 |
| W7-X | 0.51 | 5.51 | −0.127 | 0.894 | 5 | 1.11 |
| LHD | 0.60 | 3.73 | −1.230 | −0.628 | 10 | 1.00 |

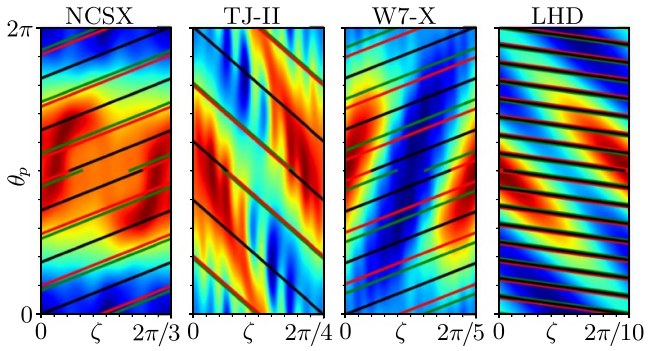


**Figure 3.** Coverage of the flux surface $r/a = 0.7$ by a field line that extends up to one (black), two (red) and three (green) poloidal turns. Only one field period is shown for each device.

simulations, where the exact length (see table 1) is chosen to ensure that $\Delta k_x = \Delta k_y$. The resolutions used for the simulations are given in appendix A, where the choices are justified by performing rigorous convergence checks of the nonlinear heat fluxes, for the different devices and gradients considered in this work.

It is important to be aware of how densely the flux surface is covered by the simulated field line, which is shown in figure 3 for field lines extending up to one (black), two (red) and three (green) poloidal turns, centered at $(\theta, \zeta) = (0, 0)$. The tokamaks are not shown, since they are axisymmetric, hence each poloidal turn is identical. Extending the field line for more than one poloidal turn samples new areas of the flux surface for W7-X. In contrast, for LHD, each additional turn overlaps almost exactly with the previous turn due to the specific value of the rotational transform on the $r/a = 0.7$ flux surface. Therefore, extending the flux tube for multiple poloidal turns does not necessarily cover additional area of the flux surface. Nonetheless, it can be important to increase the length of the flux tube to capture modes that extend beyond the first poloidal turn of the device [46], or if the parallel correlation length is longer than the length covered by one poloidal turn [26, 47, 48]. In figures 8, 11 and 19 it can be seen that the potential and heat fluxes diminish considerably at the ends, indicating that a single poloidal turn should be sufficient.

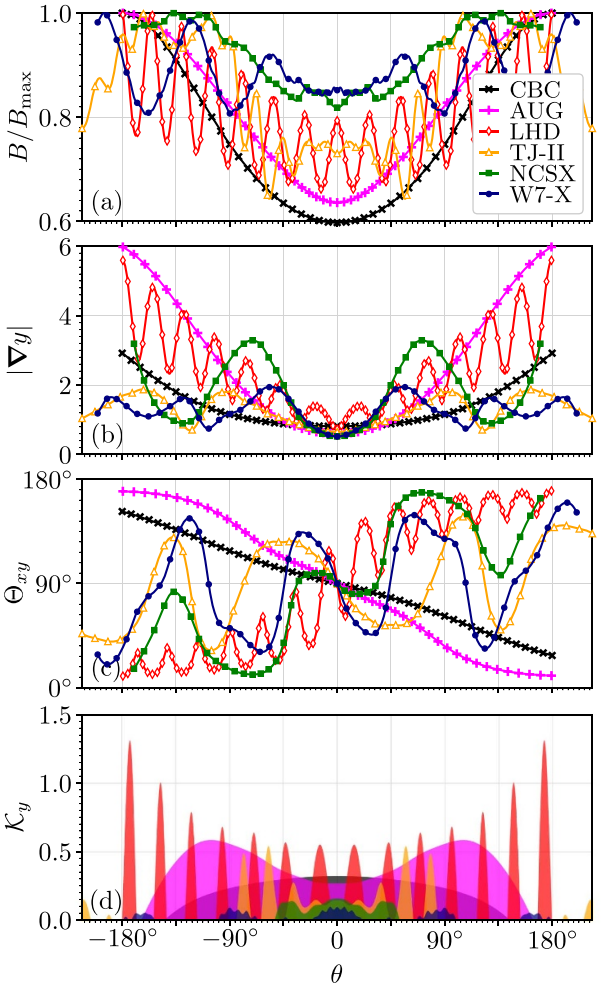


**Figure 4.** Geometric quantities along the chosen field line: (*a*) magnetic field strength normalized to its maximum along the field line, (*b*) magnitude of the perpendicular wavenumber for $k_x\rho_\mathrm{i} = 0.0$ and $k_y\rho_\mathrm{i} = 1.0$ (*c*) angle of the perpendicular cross-section $\Theta_{xy} = \arccos(\nabla x \cdot \nabla y)/(|\nabla x|\,|\nabla y|)$ and (*d*) bad curvature regions for $k_x = 0.0$ defined as $\mathcal{K}_y > 0$ with $\mathcal{K}_y = (a^2 B_r/B^3)\,\mathbf{B} \times \nabla B \cdot \nabla y$. The markers represent the parallel grid points used in the nonlinear simulations.

## 4. Localization of microinstabilities

The background density and temperature gradients can drive a large number of microinstabilities in fusion plasmas. Specifically, the ion-scale heat transport is predominately attributed to turbulence excited by ITG-driven and TEM instabilities. These instabilities are destabilized or stabilized along the magnetic field lines depending on geometric characteristics such as magnetic wells ($B$), curvature and magnetic field inhomogeneity ($\mathcal{K}_y$) and shear (whose effects are seen in $|\nabla y|$ and $\Theta_{xy}$). These characteristics, illustrated in figure 4 for the field lines considered in the nonlinear simulations, are discussed in the following paragraphs.

The magnetic shear, which gives a measure of how the rotational transform (or field line pitch) changes across neighboring flux surfaces, can have a stabilizing effect on the

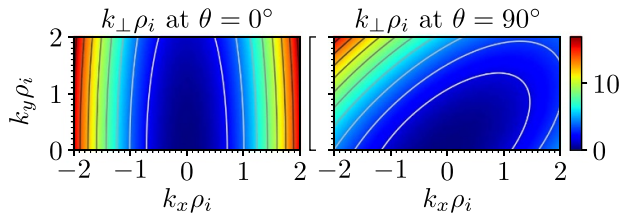


**Figure 5.** Magnitude of the perpendicular wavenumber in W7-X for the $\alpha_0 = 0$ field line centered at $(\theta,\zeta) = (0,0)$ at the parallel location $\theta = 0°$ (left) and $\theta = 90°$ (right).

instabilities. Since field-aligned coordinates are employed, the cross-section of the flux tube is twisted into a parallelogram as one moves along the field line, as a result of the local magnetic shear, which is illustrated in figure 1. The angle $\Theta_{xy}$ between $\boldsymbol{\nabla} x$ and $\boldsymbol{\nabla} y$ is depicted in figure 4(*c*). In regions where the local magnetic shear is large, the cross-section, and thus the turbulent eddies, become very twisted and are subsequently suppressed through finite-Larmor-radius (FLR) effects. The FLR-effect is enforced via the zeroth order Bessel function of the first kind, $J_0(k_\perp\rho_s)$, appearing in the gyrokinetic equation as a result of averaging out the gyrophase [49]. Here, $\mathbf{k}_\perp = k_x\boldsymbol{\nabla} x + k_y\boldsymbol{\nabla} y$ is the perpendicular wavevector and $k_\perp = (k_x^2|\boldsymbol{\nabla} x|^2 + 2k_xk_y\boldsymbol{\nabla} x\cdot\boldsymbol{\nabla} y + k_y^2|\boldsymbol{\nabla} y|^2)^{1/2}$ is its magnitude. The $J_0(k_\perp\rho_s)$-term damps small-scale fluctuations since $J_0(k_\perp\rho_s)\to 0$ for $k_\perp\rho_s \gg 1$, while large-scale fluctuations remain undamped. Therefore, an instability with wavenumbers $(\tilde{k}_x,\tilde{k}_y)$ is typically localized in regions along the field line where $k_\perp\rho_s(\tilde{k}_x,\tilde{k}_y,z)$ is minimum. Vice versa, if the strongest instability drives are found at a certain location $\tilde{z}$, then the most unstable mode, is most likely the $(k_x,k_y)$-mode that minimizes $k_\perp\rho_s(k_x,k_y,\tilde{z})$, which lies inside the inner contours shown in figure 5. Note that the FLR-damping is much stronger for ions than for electrons since $\rho_\mathrm{i} = \sqrt{m_\mathrm{e}/m_\mathrm{i}}\,\rho_\mathrm{e}$. Seeing that the center of the field line is typically chosen to have the largest instability drives, and the cross-section is taken to be rectangular in this location, the most unstable modes are generally found along $k_x = 0$ (see sections 5.1 and 6.1), because $k_x = 0$ minimizes $k_\perp\rho_s(k_x,k_y,z)$ if $\boldsymbol{\nabla} x\cdot\boldsymbol{\nabla} y = 0$. This is illustrated on the left side of figure 5. Moreover, the modes with $k_x = 0$ are confined to the center of the field line in high-shear devices. For these modes the perpendicular wavenumber reduces to $|k_y\boldsymbol{\nabla} y| \approx |k_y(r_0\boldsymbol{\nabla}\theta - r_0\iota\boldsymbol{\nabla}\zeta - \iota\hat{s}\zeta\boldsymbol{\nabla} x)|$ (figure 4(*b*)) which increases as one moves away from $\zeta = 0$. As a result, the FLR-effect confines instabilities with $k_x = 0$ to the center of the field line if the global magnetic shear $\hat{s}$ (table 1) is large. On the other hand, modes with a finite radial wavenumber $k_x \neq 0$ typically have a minimum in $k_\perp\rho_s(\tilde{k}_x,\tilde{k}_y,z)$ further along the field line, hence these modes most likely peak away from $\zeta = 0$. Therefore, it is important to include a wide range of radial wavenumbers in order to capture modes which are not excited at the center of the field line.

Besides the effects of the local and global magnetic shear, the magnetic wells, as well as the curvature and the inhomogeneity of the magnetic field, also play an important role on the localization of the instabilities. In particular, toroidal ITG modes [50] are localized in regions of bad (destabilizing) curvature, for which $k_yT_\mathrm{i}'/\psi_\mathrm{t}'(\mathbf{B}\times\boldsymbol{\nabla} B)\cdot\mathbf{k}_\perp > 0$ with $T_\mathrm{i}' = \mathrm{d}T_\mathrm{i}/\mathrm{d}r < 0$ since we only consider peaked temperature profiles and $\psi_t' = d\psi_t/dr < 0$ in the configurations considered in this work. The most unstable modes typically have $k_x = 0$ (but not always, as we will see in section 5.1) for which the condition of bad curvature reduces to $(\mathbf{B}\times\boldsymbol{\nabla} B)\cdot\boldsymbol{\nabla} y > 0$. For simplicity, we define $\mathcal{K}_y = (a^2B_r/B^3)(\mathbf{B}\times\boldsymbol{\nabla} B)\cdot\boldsymbol{\nabla} y$, and the corresponding areas of bad curvature, where $\mathcal{K}_y > 0$, are highlighted in figure 4(*d*) along the chosen magnetic field lines. Similar to ITG modes, which are destabilized by local bad curvature, TEMs [16] are driven unstable by the bounce-averaged bad curvature, which is the bad curvature that a particle trapped in a magnetic well experiences between two consecutive bounce points. Moreover, TEMs reside in regions where electrons are trapped, which is inside the magnetic wells shown in figure 4(*a*). Both the TEM and ITG mode can thus be stabilized by reducing the magnitude of the bad curvature and by reducing the connection length between regions of good and bad curvature. Moreover, the separation of regions of trapping and bad curvature has a stabilizing effect on TEMs.

Figure 6 shows the regions of particle trapping (black-red lines) and bad curvature (orange shaded areas) along the chosen magnetic field lines, for modes with $k_x = 0$, in order to discuss their overlap. Specifically, for CBC, TJ-II and NCSX, the location with the deepest magnetic well has the most pronounced bad curvature. On the other hand, in AUG and LHD these locations do not coincide. Here, the most pronounced bad curvature is found further along the field line, for $\zeta \neq 0$, because of the $\iota\hat{s}\zeta\boldsymbol{\nabla} x$ term inside $\mathcal{K}_y$. Finally, in W7-X, the central well of the chosen field line corresponds to the most pronounced bad curvature, while the deepest wells are found at $z = \pm 1.41$ (and $z = \pm 2.51$) where the curvature is comparable to the center. Since bad curvature ($\mathcal{K}_y > 0$) is destabilizing and good curvature ($\mathcal{K}_y < 0$) is stabilizing, it is important to quantify the amount of bad curvature that occurs along the field line for ITGs, while the amount of bad curvature inside the magnetic wells is decisive for TEMs. It can be seen that the field lines of the tokamaks consist almost entirely of bad curvature, since $\hat{s} = 0.8$ in CBC and $\hat{s} = 1.6$ in AUG, which increases the region of bad curvature through the $\iota\hat{s}\zeta\boldsymbol{\nabla} x$ term in $\mathcal{K}_y$, whereas the bad curvature region would be confined to the outboard side ($\theta \in [-90°, 90°]$) if $\hat{s} = 0$. When $\hat{s} < 0$, the bad curvature region is reduced, which has been shown to lead to a decrease in turbulence in tokamaks [11, 12]. In contrast, only 30%–50% of the field lines in the stellarators are covered by bad curvature. In particular, in NCSX and W7-X the magnetic wells have a considerable amount of good curvature, while in TJ-II the majority of its large magnetic well has bad curvature. Finally, in LHD the two inner magnetic wells consists almost entirely of bad curvature, whereas for the outer magnetic wells, the regions of bad curvature have been shifted with respect to the regions of trapping because of the large global magnetic shear ($\hat{s} = -1.2$).

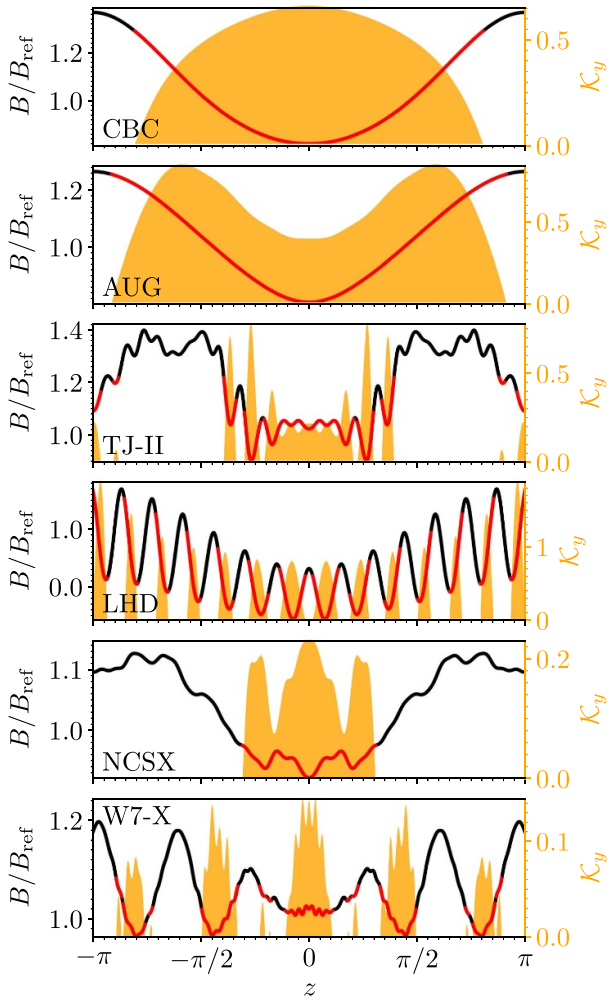


**Figure 6.** Magnetic field strength (black-red lines) and bad curvature regions ($\mathcal{K}_y > 0$, orange), where the $B$-line is colored red if it has bad curvature, and black if it has good curvature.

## 5. Linear stability analysis

Linear gyrokinetic simulations are performed for the six considered devices in order to discuss the microinstabilities that are driven unstable in the presence of various density and temperature gradients. To start, in section 5.1, scans along $(k_x, k_y)$ are performed considering $a/L_{T_\mathrm{i}} = 3.0$, $a/L_{T_\mathrm{e}} = 0.0$ and various density gradients to confirm that the most unstable mode is generally found for $k_x = 0.0$. Next, detailed scans for $0.0 \leqslant a/L_n \leqslant 4.0$ are conducted to study the evolution of the growth rate with the density gradient in section 5.2, considering $k_x = 0.0$ and limiting the binormal wavenumber to ion scales, $k_y\rho_\mathrm{i} \leqslant 2.0$. The most unstable mode is identified and discussed in section 5.3, for which the contributions of the ion temperature gradient and the density gradient are isolated in section 5.4. A vanishing electron temperature gradient is considered in the simulations to avoid the excitation of the ETG mode, which is isomorphic to the ITG mode, hence it is driven at electron scales, $k_{y,\mathrm{ETG}} = (\rho_\mathrm{i}/\rho_\mathrm{e})\, k_{y,ITG}$, and it has much larger growth rates, $\gamma_\mathrm{ETG} = (\rho_i/\rho_e)\gamma_\mathrm{ITG}$. Including electron scales is beyond the scope of this work. Nonetheless, the effect of $a/L_{T_\mathrm{e}} = 3.0$ on the ion-scale instabilities is discussed in section 5.4. Finally, in section 5.5 growth-rate maps are constructed for the six considered devices considering a wide range of gradients with $a/L_n \in [0.0, 8.0]$ and $a/L_{T_\mathrm{i}} \in [0.0, 8.0]$. It is important to note that this work is limited to the analysis of the fastest-growing mode as `stella` is an initial value solver. However, it has been shown that subdominant modes can play a crucial role on the nonlinear dynamics of the turbulence [26, 27].

### 5.1. Growth rate as a function of $k_x\rho_\mathrm{i}$ and $k_y\rho_\mathrm{i}$

Generally, linear studies of gyrokinetic simulations are performed considering a vanishing radial wavenumber, i.e. $k_x = 0.0$. This simplification is justified when the most unstable mode peaks at a location along the flux tube where the flux-tube cross-section is perpendicular, or if it peaks symmetrically around such a location. Therefore, most gyrokinetic codes ensure that the center of the flux tube has a perpendicular cross-section, i.e. $\nabla x \cdot \nabla y = 0$ at $z = 0$. Moreover, the center is typically chosen to correspond to the location with the deepest magnetic well, and the most pronounced bad curvature, as discussed in section 4. With these choices, the most unstable mode most likely peaks at the center, where it would be characterized by having $k_x = 0.0$, whereas if it would be localized further along the flux tube, at a location where the cross-section has become twisted, it is characterized by $k_x \neq 0.0$, due to the FLR-effects (see section 4). In order to verify whether the most unstable modes have $k_x = 0.0$, the growth rates $\gamma a/v_{\mathrm{th,i}}$ of the linear instabilities are shown in figure 7 as a function of $(k_x, k_y)$ for $a/L_{T_\mathrm{i}} = 3.0$, $a/L_{T_\mathrm{e}} = 0.0$ and considering a density gradient of $a/L_n = 0.0$ (left column), $a/L_n = 2.0$ (middle column) and $a/L_n = 4.0$ (right column). The corresponding frequencies $\omega a/v_{\mathrm{th,i}}$ can be found in appendix B. The perpendicular wavenumbers are restricted to ion scales, specifically, $0 \leqslant k_x\rho_\mathrm{i} \leqslant 2.0$ and $0 \leqslant k_y\rho_\mathrm{i} \leqslant 2.0$, where we limit the scans to positive $k_x$ since the field lines are stellarator-symmetric, hence the $k_x$-modes and the $-k_x$-modes have the same growth rates and frequencies, and we only consider positive $k_y$-modes because of the reality condition. The length of the flux tube is restricted to one poloidal turn in this section.

For the three considered density gradients, the most unstable mode, which is highlighted by a white cross in figure 7, is indeed found at $k_x = 0.0$ in CBC, AUG, NCSX, LHD and TJ-II. For W7-X, when considering low density gradients, the most unstable mode is also found at $k_x\rho_\mathrm{i} = 0.0$. However, when the density gradient is increased to $a/L_n = 4.0$, the most unstable mode is instead found at $k_x\rho_\mathrm{i} = 1.0$ and $k_y\rho_\mathrm{i} = 1.375$. Specifically, for $a/L_n = 4.0$, the growth rate at $k_x\rho_\mathrm{i} = 0.0$ and $k_y\rho_\mathrm{i} = 0.5$ is 13% smaller than at $k_x\rho_\mathrm{i} = 1.0$ and $k_y\rho_\mathrm{i} = 1.375$. As explained in section 4, the most unstable mode is most likely excited at the center for W7-X, but it can also be excited in the magnetic wells at $z = \pm 1.41$ (figure 6) due to the depth of the magnetic well and the strength of the bad curvature at this location. At $z = \pm 1.41$ the cross-section has become sheared and the most unstable mode corresponds to the $(k_x, k_y)$-mode for which the FLR-damping

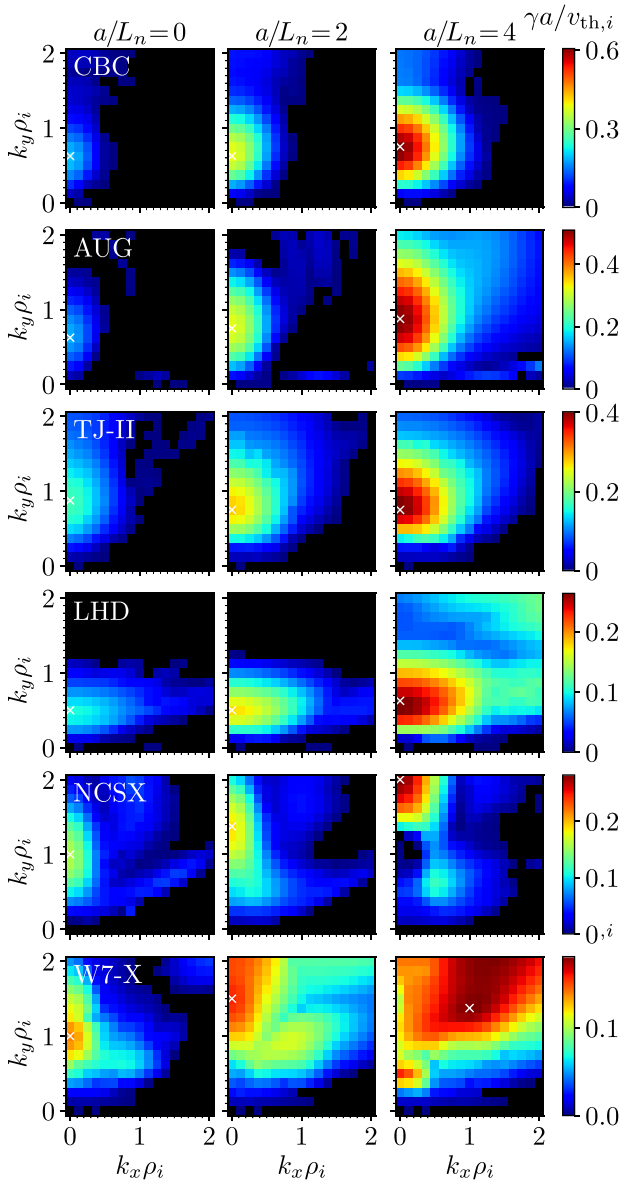


**Figure 7.** Normalized growth rate as a function of $(k_x\rho_\mathrm{i}, k_y\rho_\mathrm{i})$ for $a/L_{T_\mathrm{i}} = 3.0$, $a/L_{T_\mathrm{e}} = 0.0$ and $a/L_n = 0.0$ (left column), $a/L_n = 2.0$ (middle column) and $a/L_n = 4.0$ (right column). The most unstable mode is highlighted with a white cross.

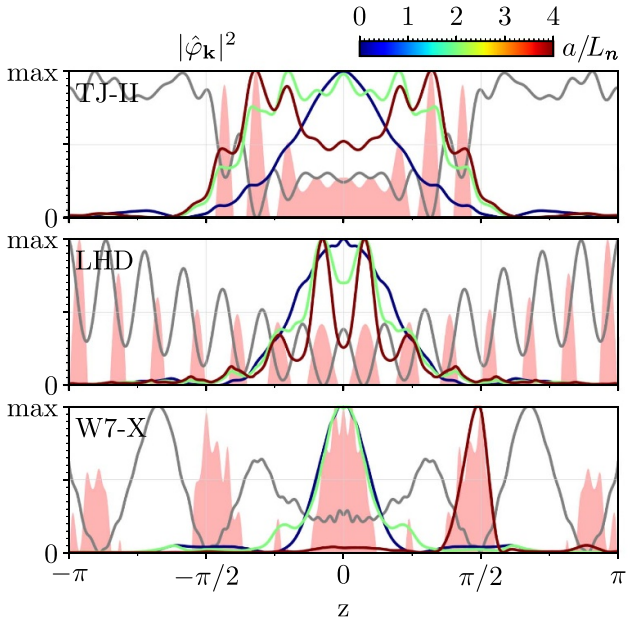


**Figure 8.** Potential squared along the magnetic field line, for the most unstable mode (white crosses) of figure 7. The strength of the magnetic field is shown in gray, regions of bad curvature are highlighted in red, and the colors of the parallel mode structures correspond to the $a/L_n$-scale shown on top.

is the smallest, which is inside the inner contour shown on the right-hand-side of figure 5.

In CBC, AUG and NCSX the most unstable mode peaks at the center of the flux tube where the cross-section is perpendicular, hence it has $k_x = 0.0$. On the other hand, in TJ-II and LHD, for $a/L_n = \{2.0, 4.0\}$, the mode with $k_x = 0.0$ peaks symmetrically around the center of the flux tube, in the two magnetic wells at $z = \pm 0.23$ for LHD, and in the magnetic wells at $z = \pm 0.54$ and $z = \pm 0.83$ for TJ-II. This is illustrated in figure 8 by plotting the parallel mode structure of the most unstable mode, corresponding to the white crosses in figure 7. Finally, in W7-X, the most unstable mode has $k_x\rho_\mathrm{i} \neq 0.0$ for $a/L_n = 4.0$, for which the mode peaks in the magnetic well at $z = 1.41$.

To conclude, if the cross-section at the center of the flux tube is chosen to be perpendicular and if it corresponds to the location with the strongest instability drives, then the most unstable mode is generally found for $k_x\rho_\mathrm{i} = 0.0$. However, in some cases, the most unstable mode is characterized by $k_x\rho_\mathrm{i} \neq 0.0$, because the mode peaks further along the flux tube, at a location where the cross-section has become sheared. It is important to note that in nonlinear simulations, all the fastest-growing $(k_x, k_y)$-modes shown in figure 7, as well as the subdominant modes (which are not computed in this work), are coupled and will influence the nonlinear saturation of the turbulence [51].

### 5.2. Growth rate as a function of $a/L_n$ and $k_y\rho_\mathrm{i}$

The linear analysis is continued considering $k_x\rho_\mathrm{i} = 0.0$, while scanning $k_y\rho_\mathrm{i}$ in $[0.125, 2.0]$ to investigate the perpendicular scale of the modes. We simultaneously scan $a/L_n$ in $[0.0, 4.0]$ to study the evolution of the instabilities as the density gradient is increased. An ion temperature gradient of $a/L_{T_\mathrm{i}} = 3.0$ and a vanishing electron temperature gradient $(a/L_{T_\mathrm{e}} = 0.0)$ are considered. The flux tube is extended up to three poloidal turns in order to capture extended modes. The growth rates and frequencies of the modes are shown in figure 9. Note that negative frequencies correspond to modes traveling in the electron diamagnetic direction, while those with positive frequencies travel in the ion diamagnetic direction.

In CBC, AUG, TJ-II and LHD, the linear instabilities become increasingly more unstable with increasing density gradients. Considering the range of scanned density gradients,

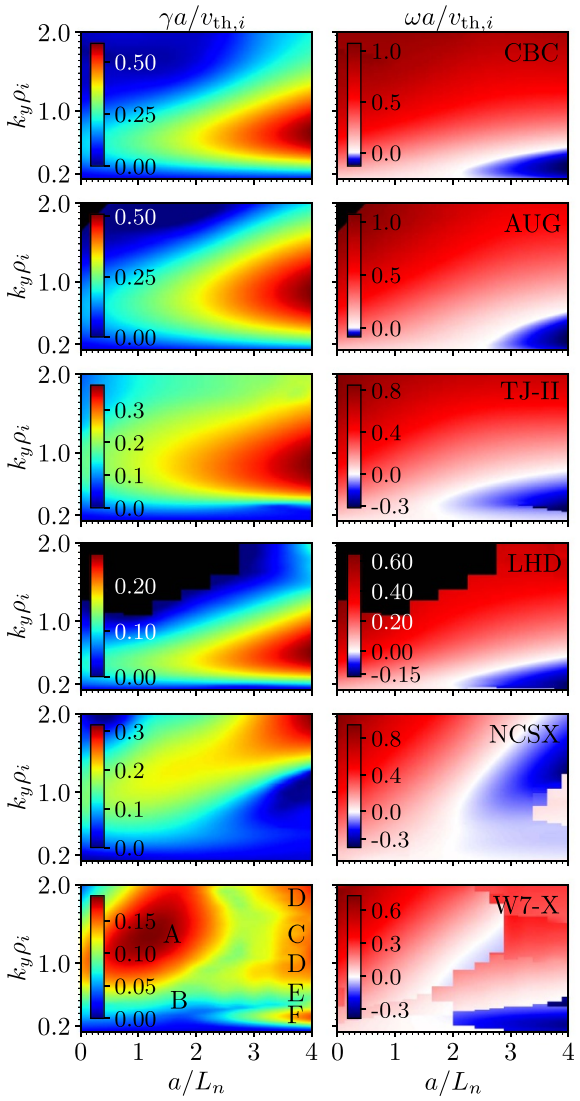


**Figure 9.** Normalized growth rate (left) and frequency (right) as a function of the normalized density gradient, and the binormal wavenumber, considering $k_x\rho_\mathrm{i} = 0.0$, $a/L_{T_\mathrm{i}} = 3.0$ and $a/L_{T_\mathrm{e}} = 0.0$. The frequency branches in W7-X are labeled A–F.

it is expected that distinct analytical instabilities are present in these devices. Specifically, ITG modes should be dominant at $a/L_n = 0.0$ and density-gradient-driven instabilities such as TEMs, iTEMs and universal instabilities should be present at $a/L_n = 4.0$, where it is likely that they are mixed with the ITG mode due to the presence of the strong ion temperature gradient of $a/L_{T_\mathrm{i}} = 3.0$. It can be seen that CBC, AUG, TJ-II and LHD have continuous frequency maps, except for very small $k_y\rho_\mathrm{i}$ in LHD and TJ-II. This continuous change of the frequency is accompanied by a continuous change of the parallel mode structure of these modes, which is discussed in detail for the most unstable mode along $k_y\rho_\mathrm{i}$ in the next section (figure 11). These continuous frequency branches indicate that the modes are transforming into one another through a continuous change of the density gradient [52]. As a result, one should refrain from labeling modes traveling in the ion diamagnetic direction as ITG modes, and those traveling in the electron diamagnetic direction as TEM modes, since in the presence of both $a/L_n$ and $a/L_{T_\mathrm{i}}$ the modes are most likely mixed to a certain degree.

In contrast, the growth rate and frequency spectra of NCSX and W7-X are very different. Specifically, in NCSX, the growth rate also increases with increasing density gradients, however, the most unstable mode migrates to larger $k_y\rho_\mathrm{i}$, in contrast to the other five devices. According to mixing length arguments, where $Q_\mathrm{i} \propto \gamma/k_y^2$, one could expect the heat transport to be reduced as the density gradient increases because the perpendicular scale of the modes becomes smaller, although it has been demonstrated that reliable quasi-linear models must account for all subdominant unstable modes [53]. Moreover, note that a second instability with positive frequencies shows up at large density gradients. On the other hand, the growth rate spectrum of W7-X consists of multiple different peaks, which correspond to six distinct frequency branches, characterized by having different parallel mode structures (shown for the most unstable mode along $k_y\rho_\mathrm{i}$ in figure 11). For the highest density gradient, $a/L_n = 4.0$, four distinct instability branches co-exist within $k_y\rho_\mathrm{i} \leqslant 2.0$. The different branches have been labeled (A) to (F). In W7-X, the growth rate thus initially increases with the density gradient until $a/L_n = 1.25$, after which the growth rate decreases up to $a/L_n = 2.75$, due to the stabilization of instability (A) by increasing density gradients—which is most likely an ITG mode—without driving the other instabilities particularly unstable yet. As the density gradient is increased further, the instabilities corresponding to frequency branches (C) to (F) appear, which are driven unstable by the density gradient. Note that instability (F) has large perpendicular wavelengths, hence it could be particularly detrimental to the heat transport.

In summary, CBC, AUG, TJ-II and LHD have continuous frequency spectra, where the modes undergo a smooth transition from one instability into another as the density gradient is increased, whereas NCSX and W7-X are characterized by abrupt transitions between different frequency branches. Hence, it is clear that in most cases, a frequency branch does not necessarily correspond to a distinct analytical instability such as the ITG or TEM, and the identification of the instabilities should be done very carefully or be avoided altogether.

### 5.3. *Most unstable mode as a function of* $a/L_n$

Next, the growth rate, frequency and wavenumber of the most unstable modes of figure 9 are plotted as a function of the density gradient in figure 10, which is a linear analysis commonly performed in gyrokinetic studies. Recall that we consider $a/L_{T_\mathrm{i}} = 3.0$, $a/L_{T_\mathrm{e}} = 0.0$, $k_x\rho_\mathrm{i} = 0.0$ and $k_y\rho_\mathrm{i} \leqslant 2.0$. For CBC, AUG, TJ-II and LHD, the growth rate of the most unstable mode increases approximately linearly with the density gradient (figure 10(*a*)), while there is no significant change in the perpendicular scales of the modes (figure 10(*c*)). In NCSX, the growth rate also increases as the density gradient is increased, however, it has a weaker dependence on $a/L_n$. Additionally, the perpendicular scales of the modes become

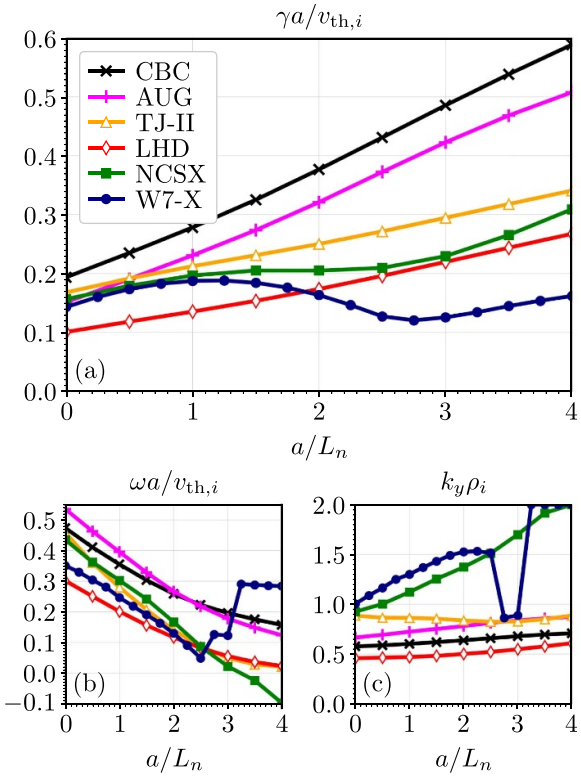


**Figure 10.** The ($a$) normalized growth rate, ($b$) normalized frequency, and ($c$) normalized binormal wavenumber of the most unstable mode as a function of the normalized density gradient, $a/L_n$, considering $k_x = 0.0$, $a/L_{T_\mathrm{i}} = 3.0$ and $a/L_{T_\mathrm{e}} = 0.0$.

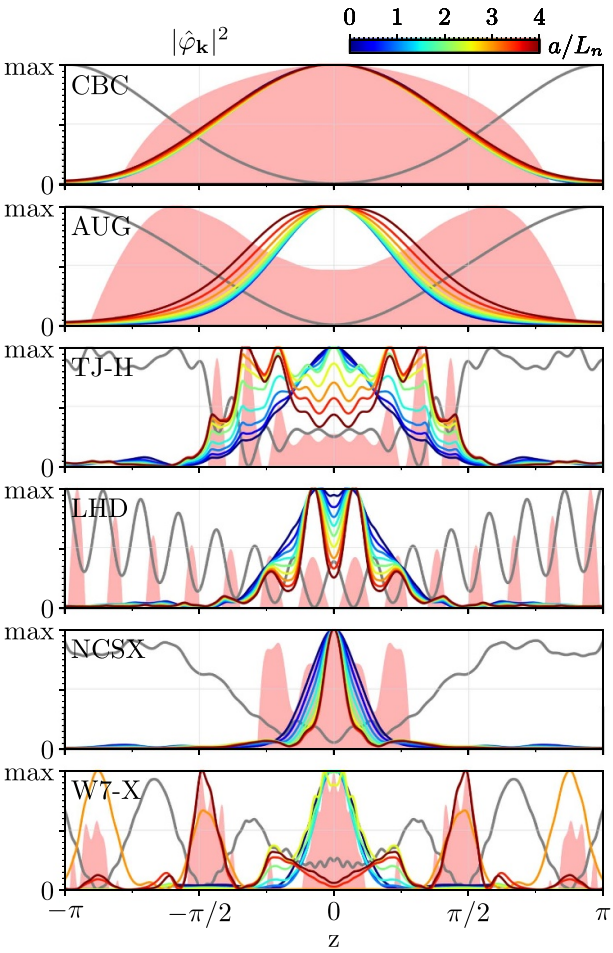


**Figure 11.** Potential squared along the magnetic field line, for the modes in figure 10. The strength of the magnetic field is shown in gray, regions of bad curvature are highlighted in red, and the colors of the parallel mode structures correspond to the $a/L_n$-scale shown on top.

smaller. In contrast, in W7-X, the growth rates are reduced by 36% from $a/L_n = 1.25$ to $a/L_n = 2.75$. A similar trend is observed when considering the most unstable mode for $k_x\rho_\mathrm{i} \leqslant 2.0$ and $k_y\rho_\mathrm{i} \leqslant 2.0$ in W7-X (not shown here). A decrease in the perpendicular scales of the modes is also observed in W7-X in figure 10($c$), however, this is misleading since figure 9 indicates that multiple instabilities co-exist at high density gradients, some of which are characterized by having large perpendicular scales. Therefore, one has to be careful when interpreting linear results based only on the most unstable $(k_x, k_y)$-mode. Nonetheless, the linear analysis suggest that a reduction of the heat transport with increasing density gradients is expected for NCSX and W7-X based on mixing length arguments, $Q_i \propto \gamma/k_y^2$, while an increase is expected for CBC, AUG, TJ-II and LHD.

In order to explain the differences in the linear behavior between these devices, $|\hat{\varphi}_{\mathbf{k}}|^2$ is plotted along the field line in figure 11, for the modes from figure 10. These parallel mode structures give insight into the geometric characteristics that drive the instability. In every device, except for LHD, the modes peak at the center of the field line for small density gradients, where the ITG mode is believed to be dominant, which is driven unstable in bad curvature regions (figure 4($d$)). This is mainly due to the FLR-damping, which scales with $k_\perp\rho_\mathrm{i}$ for the ions, and has a minimum at the center of the flux tube for $k_x = 0.0$ (figure 4($b$)). On the other hand, as the density gradient is increased, the modes become localized inside the deepest magnetic wells, since TEMs start having a significant influence. Specifically, CBC and AUG have a single magnetic well consisting of mostly bad curvature, hence the modes have the same parallel mode structure regardless of the density gradient. On the other hand, in LHD, the modes become more localized inside the magnetic wells as the density gradient is increased since trapped electrons start driving the instabilities. Note that the modes are more localized (the mode structures are more narrow) in AUG ($\hat{s} = 1.6$) and LHD ($\hat{s} = 1.2$) compared to CBC ($\hat{s} = 0.8$), due to the higher global shear and thus stronger FLR-damping towards the ends of the flux tube. NCSX shows improved confinement of the modes, despite the moderate global shear ($\hat{s} = 0.7$) which is likely due to the very strong local magnetic shear (figure 4($b$)). This limits the modes to a region which is even smaller than the already quite narrow region of bad curvature. In contrast, the mode structures in TJ-II are quite broad, since the shear is low and there is a large central well which consists almost entirely of bad curvature. Finally, in W7-X, distinct mode structures occur,

corresponding to distinct frequency branches (figure 10). For low density gradients, the modes peak at the center where the FLR-damping is the weakest and the bad curvature is the largest (figures 4(*b*) and (*d*)). Whereas for $a/L_n = 3.0$ the mode peaks inside the wells at $z = \pm 2.51$, and for $a/L_n \geqslant 3.5$ the modes peak in the wells at $z = \pm 1.41$.

Moreover, the magnetic geometry is correlated to the magnitude of the growth rates of the instabilities. Specifically, in the devices where the mode structures are confined to narrow regions of the field line, such as in LHD, NCSX and W7-X, the growth rates are the smallest (figure 10). Additionally, the high local magnetic shear in NCSX, and the intermittent regions of bad and good curvature in the central well of W7-X have a stabilizing effect. TJ-II has the largest growth rates of the stellarators due to its low shear and broad magnetic well, which is covered almost entirely by bad curvature. Finally, the tokamaks have the highest growth rates since most of the field line is driving the modes unstable, where AUG performs slightly better, most likely due to its higher shear.

### *5.4. Separate contributions to the growth rate from the ion temperature gradient and the density gradient*

In most devices, we are unable to distinguish between different instability types, since the transitions between them are smooth (section 5.2). Nonetheless, it is possible to isolate specific instabilities based on their instability drive by modifying the simulations accordingly, which is shown in figure 12. The original simulations considered in figure 10 are reproduced here with black lines. Firstly, we consider the case of adiabatic electrons to isolate the instabilities which are driven by the ion temperature gradient and which rely solely on the ion dynamics (blue dashed lines). Next, we impose vanishing temperature gradients while treating the electrons kinetically, to isolate modes which are driven by the density gradient and require electron dynamics (red dotted lines).

The instabilities driven by the ions (blue dashed lines) show an initial increase in their growth rates with the density gradient until $a/L_n = 1.0$, after which the growth rates decrease, and eventually the instability is suppressed by the density gradient. The plasma parameters and behavior of these modes suggest that this instability corresponds to the toroidal ITG mode [50]. The density gradient for which these modes are suppressed is the highest in CBC, AUG, TJ-II and LHD, and the lowest in NCSX and W7-X. Moreover, note that for $a/L_n = 0.0$, including the electron dynamics (blue lines $\rightarrow$ black lines) has a destabilizing effect in every device, except in NCSX and W7-X, where it has no effect on the growth rate.

The red dotted line in figure 12 represents the contribution of the density-gradient-driven modes, which are most likely TEMs [16] or iTEM [54] but they could also be passing-particle-driven universal instabilities [55, 56], however this instability is typically subdominant to TEMs. A minimum density gradient is required in order to drive these modes unstable, after which the growth rate increases with the density gradient. Note that for high density gradients in W7-X, TJ-II and AUG, the linear growth rates are reduced by the presence

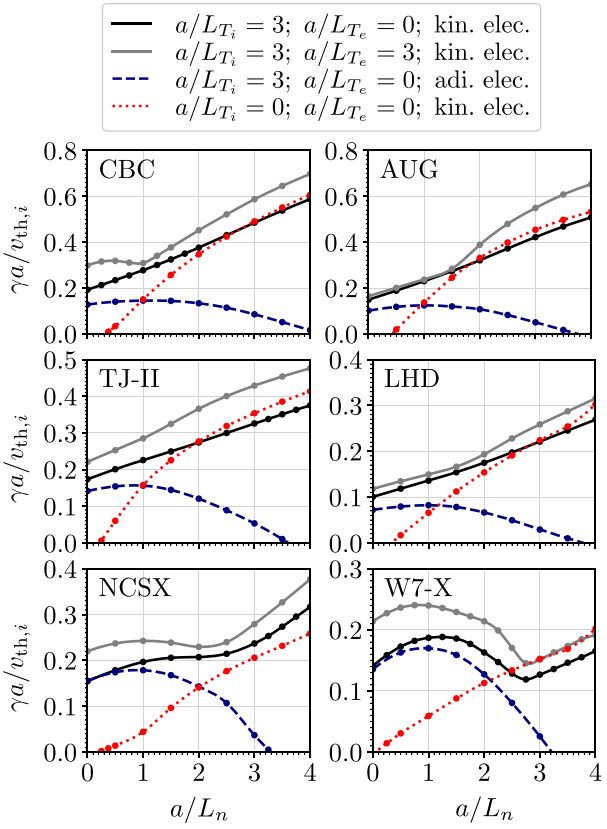


**Figure 12.** Normalized growth rate as a function of the normalized density gradient with kinetic electrons, $a/L_{T_i} = 3$ and a vanishing electron temperature gradient (black), and with $a/L_{T_e} = 3$ (gray). Ion-temperature-gradient-driven modes are isolated by treating the electrons as adiabatic (blue) and density-gradient-driven modes are isolated by setting $a/L_{T_i} = 0$ (red).

of an ion temperature gradient (red lines $\rightarrow$ black lines), in contrast to NCSX, where the ion temperature gradient has a destabilizing effect.

In CBC, AUG, TJ-II and LHD the growth rates of the modes in the presence of both the ion temperature gradient and kinetic electrons (black lines) increase monotonously with the density gradient. In contrast, in W7-X, and to lesser extent in NCSX, distinct instabilities are observed in the frequency spectra (figure 9), and the growth rates of the original simulations (black lines) resembles the sum of the growth rates of the ITG-driven modes (blue lines) and the density-gradient-driven modes (red lines). The presence of a clear separation between these two contributions is related to the density gradient above which the growth rates driven solely by the density-gradient-driven modes exceeds those driven by the ITG-driven modes, i.e. where the red line crosses the blue line. This occurs at around $a/L_n \approx 1.0$ for CBC, AUG, TJ-II and LHD, whereas it occurs around $a/L_n \approx 2.0$ for NCSX and W7-X. Hence, in NCSX and W7-X, there is a clear separation between these two instabilities, and there is a region of density gradients for which the ITG-driven modes are stabilized by the density gradient, without driving the density-gradient-driven modes particularly unstable yet.

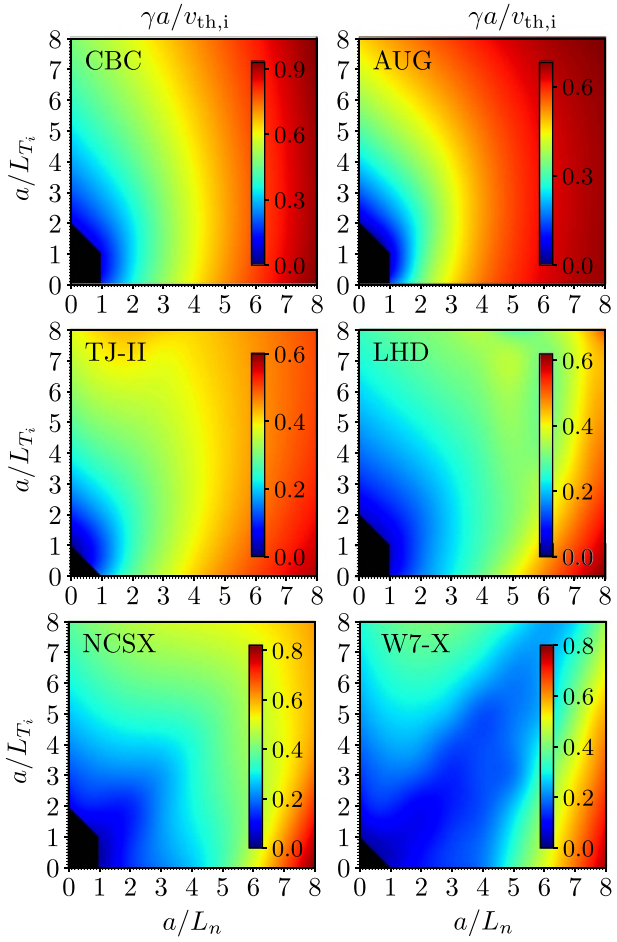


**Figure 13.** Normalized growth rate of the most unstable mode for $k_x\rho_\mathrm{i} = 0.0$ and $k_y\rho_\mathrm{i} \leqslant 2.0$, as a function of the normalized density gradient and the normalized ion temperature gradient, for a vanishing electron temperature gradient.

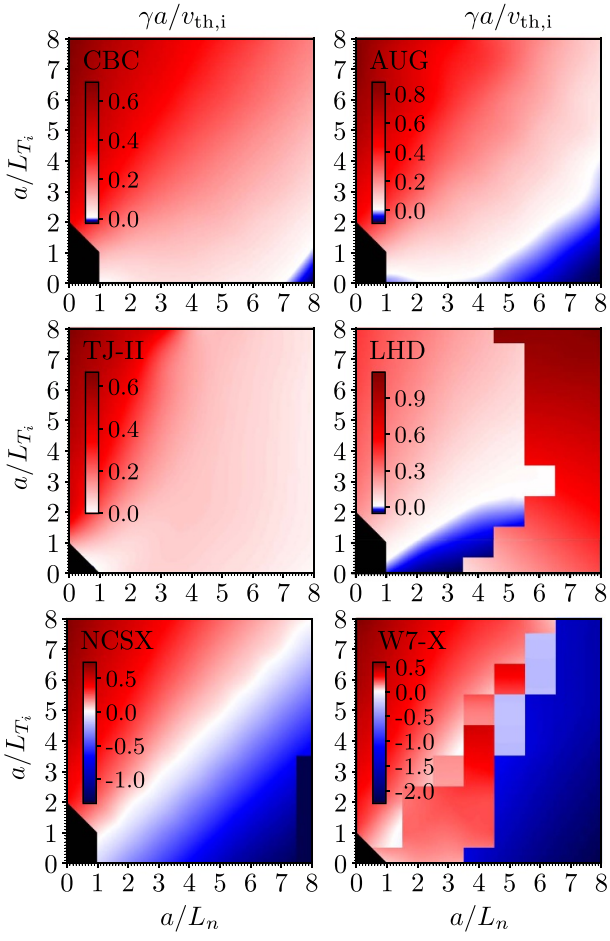


**Figure 14.** Normalized frequency of the most unstable mode for $k_x\rho_\mathrm{i} = 0.0$ and $k_y\rho_\mathrm{i} \leqslant 2.0$, as a function of the normalized density gradient and the normalized ion temperature gradient, for a vanishing electron temperature gradient.

Finally, the effect of adding a non-vanishing electron temperature gradient, set to $a/L_{T_\mathrm{e}} = a/L_{T_\mathrm{i}} = 3.0$, is represented by the gray lines in figure 12. It can be seen that the presence of an electron temperature gradient increases the growth rates in every device, hence it has a destabilizing effect on the ion-scale instabilities. Note that in CBC the ETG mode is dominant for $a/L_n \leqslant 0.75$, since the most unstable mode is found at the end of the scanned wavenumber range, at $k_y\rho_\mathrm{i} = 2.0$, and it propagates in the electron diamagnetic direction (not shown here). Increasing the scanned $k_y\rho_\mathrm{i}$-values shows that this mode belongs to the ETG branch which peaks at electron scales.

### 5.5. Growth rate as a function of $a/L_n$ and $a/L_{T_\mathrm{i}}$

The linear analysis is extended to a wide range of plasma parameters, varying the gradients from flat density and ion temperature profiles ($a/L_n = 0.0$ and $a/L_{T_\mathrm{i}} = 0.0$) up to extremely peaked profiles ($a/L_n = 8.0$ and $a/L_{T_\mathrm{i}} = 8.0$), scanned with a step of $a/L_n = 1.0$ and $a/L_{T_\mathrm{i}} = 1.0$, while considering a vanishing electron temperature gradient ($a/L_{T_\mathrm{e}} = 0.0$). The growth rates and frequencies of the most unstable modes, found for $k_x\rho_\mathrm{i} = 0.0$ and $k_y\rho_\mathrm{i} \leqslant 2.0$, are shown in figures 13 and 14, respectively. The wavenumber of the most unstable mode is discussed in appendix C. These maps contribute to the collection of growth-rate maps for various configurations presented in [57]. Note that the black regions indicate that no unstable modes were found within the considered CPU time. Resolving these modes, which lie near marginality, would require a more extensive study. Moreover, it is important to acknowledge that for most devices, the gradients that are considered in this section are far beyond the experimentally relevant values at $r/a = 0.7$. Therefore, one needs to be careful when drawing conclusions based on such extreme scans.

It is clear that W7-X is the only device which exhibits a prominent valley [57], i.e. a region along the diagonal $a/L_n \approx a/L_{T_\mathrm{i}}$ which is characterized by having significantly reduced growth rates (figure 13). However, note that for the specific choice of $a/L_{T_\mathrm{i}} = 3.0$ and $a/L_n \leqslant 4.0$, the reduction of the growth rate in W7-X is very modest (figure 10). As explained in the previous section, this valley in W7-X is formed by the stabilization of the ITG-driven modes by increasing density gradients, without driving the density-gradient-driven modes particularly unstable yet. Similarly, a small reduction of the growth rate is observed along $a/L_n \approx$

$a/L_{T_\mathrm{i}}$ in NCSX, while for the other four devices, no reduced growth rates are observed along the diagonal.

In figure 14, the frequency of the most unstable mode is depicted. Each frequency branch, whose modes have a similar parallel mode structure and occur at a similar binormal wavenumber (see appendix C), has been interpolated separately. In CBC, AUG, TJ-II, and NCSX the most unstable mode changes continuously from a pure ITG-driven mode (top left) to a pure density-gradient-driven mode (bottom right), as can be seen by the continuous change of the frequency throughout all scanned gradients—except for the jump to a new frequency branch at $a/L_n = 8.0$ for NCSX. On the other hand, LHD exhibits a similar frequency map as the other devices for low density gradients, while for high density gradients, the most unstable mode belongs to a different frequency branch, which is characterized by a different parallel mode structure (see appendix C). In contrast, many distinct instabilities live inside the growth-rate valley of W7-X.

In summary, the linear analysis at $a/L_{T_\mathrm{i}} = 3.0$ reveals a modest reduction of the growth rates with increasing density gradients in W7-X and the absence of large-scale modes at high density gradients in NCSX (figure 9), indicating a potential reduction of nonlinear heat transport with increased density gradients. In contrast, in CBC, AUG, TJ-II and LHD the linear observations point towards an increase of the heat transport with increasing density gradients, since the growth rates increase with $a/L_n$, and the perpendicular scale of the turbulence remains large. Moreover, analyzing the geometric characteristics of the chosen field line, it is evident that the modes in NCSX and W7-X are confined to narrow regions along the field lines, due to the high local magnetic shear in NCSX and due to the narrow magnetic wells and regions of bad curvature in W7-X (figure 11).

## 6. Nonlinear analysis

In the final part of this paper, nonlinear simulations are performed to investigate the effect of density gradients on turbulence. Section 6.1 provides a detailed discussion on the ion heat transport, while section 6.2 isolates the contributions from the ITG-driven modes and the density-gradient-driven modes. Next, section 6.3 examines the electron heat flux, addressing the influence of a non-vanishing electron temperature gradient. Finally, more insight is given into the characteristics of the instabilities that drive the turbulence in section 6.4, by identifying the contribution of the trapped and passing particles to the turbulent distribution function. The resolution used for these simulations is provided in table 7, and extensive resolution checks are performed in appendix A.

### 6.1. Turbulent heat transport

In the following sections, we will discuss the ion and electron heat fluxes, $Q_\mathrm{i}$ and $Q_\mathrm{e}$, which are normalized with respect to the ion gyro-Bohm flux, defined as $Q_\mathrm{g}B,i = n_\mathrm{i} T_\mathrm{i} v_{\mathrm{th,i}} (\rho_\mathrm{i}/a)^2$. The precise definition of the heat flux in the context of flux-tube simulations is given by equation (5.2) in [32]. The evolution of the ion heat flux as a function of the normalized density gradient, considering $a/L_{T_\mathrm{i}} = 3.0$ and $a/L_{T_\mathrm{e}} = 0.0$, is shown in figure 15, and summarized in table 2.

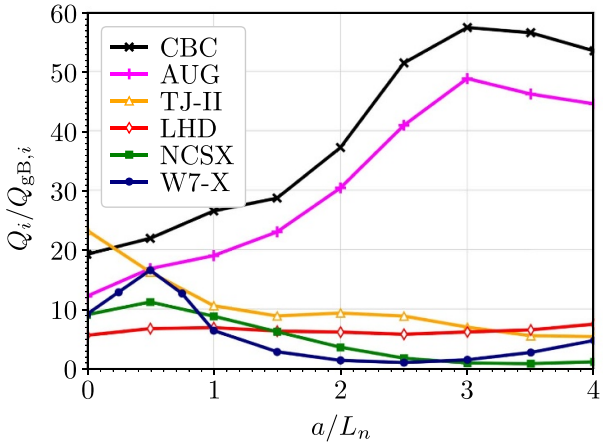


**Figure 15.** Ion heat flux as a function of the normalized density gradient, considering $a/L_{T_\mathrm{i}} = 3.0$ and $a/L_{T_\mathrm{e}} = 0.0$.

**Table 2.** Time-averaged ion heat fluxes, $Q_\mathrm{i}/Q_{\mathrm{gB},i}$, considering $a/L_{T_\mathrm{i}} = 3.0$ and $a/L_{T_\mathrm{e}} = 0.0$, corresponding to the data in figures 15 and 16, as well as the black curves in figure 21.

| | $a/L_n = 0$ | $a/L_n = 1$ | $a/L_n = 2$ | $a/L_n = 3$ |
|---|---|---|---|---|
| CBC | 19.2 | 26.5 | 37.2 | 57.4 |
| AUG | 12.1 | 19.0 | 30.4 | 48.8 |
| TJ-II | 23.3 | 10.6 | 9.3 | 7.0 |
| LHD | 5.6 | 6.9 | 6.1 | 6.1 |
| NCSX | 9.0 | 8.8 | 3.6 | 0.9 |
| W7-X | 9.1 | 6.4 | 1.4 | 1.5 |

For the tokamak configurations, the density gradient gives rise to a significant increase of the ion heat transport, up to $a/L_n = 3.0$, after which it decreases slightly. In order to discuss the stellarators, a zoom of the this plot is shown in figure 16. For LHD, the ion heat flux is approximately independent of the density gradient. On the other hand, in TJ-II the ion heat flux is reduced significantly for $a/L_n \leqslant 1.5$ and $a/L_n \geqslant 2.5$, whereas it remains approximately constant within $1.5 \leqslant a/L_n \leqslant 2.5$. In contrast, in NCSX and W7-X, a very strong reduction of the ion heat flux is observed across a wide range of density gradients. Initially, the ion heat flux increases for $a/L_n \leqslant 0.5$, after which there is a reduction of the ion heat flux by an order of magnitude in both devices. Note that the ion heat flux starts increasing again for $a/L_n \geqslant 2.5$ in W7-X and for $a/L_n \geqslant 3.5$ in NCSX.

Comparing the nonlinear ion heat fluxes with the linear growth rates in figure 10(*a*), it is clear that the reduction of the ion heat flux in W7-X is an order of magnitude stronger than the reduction of the growth rates. Moreover, the ion heat flux in NCSX is reduced very strongly, while the growth rates do not indicate any reduction. For LHD and TJ-II the growth rates increase linearly with the density gradient, while their ion heat flux is either constant or gets reduced. Even when taking into account the perpendicular scale of the modes observed

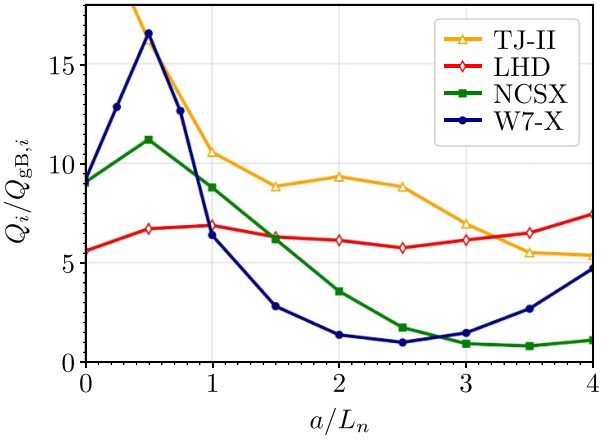


**Figure 16.** Ion heat flux as a function of the normalized density gradient, for $a/L_{T_\mathrm{i}} = 3.0$ and $a/L_{T_\mathrm{e}} = 0.0$ (zoom of figure 15).

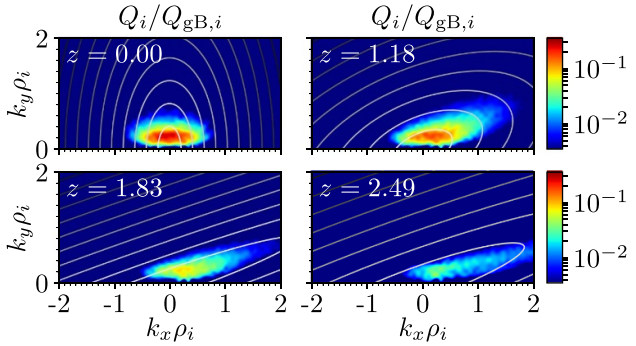


**Figure 17.** Contributions of the individual $(k_x, k_y)$-modes to the ion heat flux of LHD, for different points along the field line considering $a/L_n = 4.0$, $a/L_{T_\mathrm{i}} = 3.0$ and $a/L_{T_\mathrm{e}} = 0.0$. The contour lines represent the magnitude of the perpendicular wavenumber $k_\perp\rho_\mathrm{i}$ (white is minimum, black is maximum).

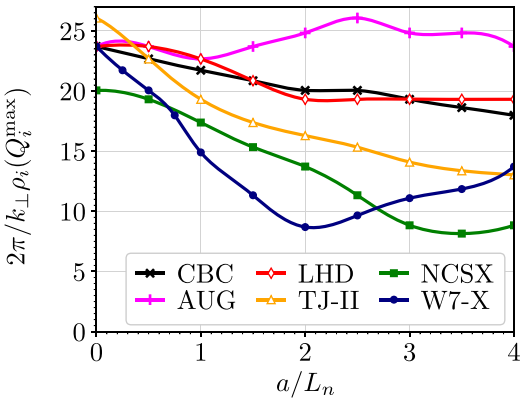


**Figure 18.** Dominant perpendicular scale of the fluctuations that contribute to the ion heat flux, for $a/L_{T_\mathrm{i}} = 3.0$ and $a/L_{T_\mathrm{e}} = 0.0$.

in the linear simulations (figure 10(*c*)), the reduction of the ion heat flux in NCSX and W7-X is much larger than the reduction of $\gamma/k_y^2$. Therefore, it is clear that there is no correlation between the nonlinear ion heat fluxes and the linear growth rates of the fastest-growing modes for the stellarators. The fastest-growing mode is thus not necessarily representative of the nonlinear dynamics of the turbulence. Instead, nonlinear saturation mechanisms play a crucial role on the heat transport within these devices. Determining these underlying mechanisms, which includes the role of subdominant modes through the nonlinear transfer of energy from unstable to damped modes [51, 58–60] and the effects of zonal flow shearing and energy cascades to dissipative scales [61–63], is beyond the scope of this work. Nonetheless, NCSX and W7-X are the only two stellarators for which the linear analysis of the fastest-growing mode points towards a reduction of the nonlinear heat transport, albeit the magnitude of the reduction was significantly underestimated. On the other hand, for the tokamaks, the increase of the ion heat flux is in agreement with the increase of the growth rates for $a/L_n \leqslant 3.0$.

The contributions of the specific $(k_x, k_y)$-modes to the ion heat flux of LHD are shown in figure 17 for four different locations along the field line, in order to illustrate the effect of the local magnetic shear and FLR-damping. As can be seen in figure 19, the largest contributions to the heat flux tend to originate from the center of the field line. At $z = 0$ the cross-section of the flux tube is perpendicular and the minimum perpendicular wavenumber $k_\perp\rho_\mathrm{i}$ occurs for $k_x = 0.0$ (see section 4). As one moves along the field line, the cross-section becomes sheared (figure 4(*c*)), and the turbulent eddies become very twisted and are subsequently suppressed through the FLR-effects, leading to a reduction in heat losses towards the ends of the flux tube, as can be seen in figure 17. Note that the modes that contribute the most to the heat flux are those for which the perpendicular wavenumber $k_\perp\rho_\mathrm{i}$ is minimum—corresponding to the modes within the inner contour line—where the FLR-damping is the weakest. Seeing that the heat flux typically peaks at the center of the field line, the largest contributions thus arise from the $k_x = 0.0$ modes. For this reason, the bad curvature regions are shown for $k_x = 0.0$ in figure 19. Nonetheless, other $k_x$-modes can also contribute significantly to the heat flux, for which the bad curvature regions are located elsewhere.

The contributions $Q_\mathrm{i}(k_x, k_y, z)$ to the ion heat flux are transformed to $Q_\mathrm{i}(k_\perp\rho_\mathrm{i})$, and the $k_\perp\rho_\mathrm{i}$ for which $Q_\mathrm{i}(k_\perp\rho_\mathrm{i})$ is maximum is considered the dominant scale of the perpendicular fluctuations of the turbulence, which is shown in figure 18 as $2\pi/k_\perp\rho_\mathrm{i}(Q_\mathrm{i}^{\max})$. For W7-X, NCSX, and to lesser extent for TJ-II, the perpendicular fluctuations become significantly smaller as the density gradient increases. Moreover, the trend of $2\pi/k_\perp\rho_\mathrm{i}$ for W7-X, NCSX and TJ-II is very similar to the trend of their ion heat fluxes (figure 16), hence the heat losses are reduced partly because the scale of the turbulence becomes smaller. In contrast, for CBC and AUG the scale of the turbulence is not correlated to the trend of the ion heat flux, while in LHD both the ion heat flux and the scale of the fluctuations are approximately independent of the density gradient.

The contribution to the ion heat flux coming from specific points along the field line is visualized in figure 19. In every device, except for W7-X, the localization of the ion heat

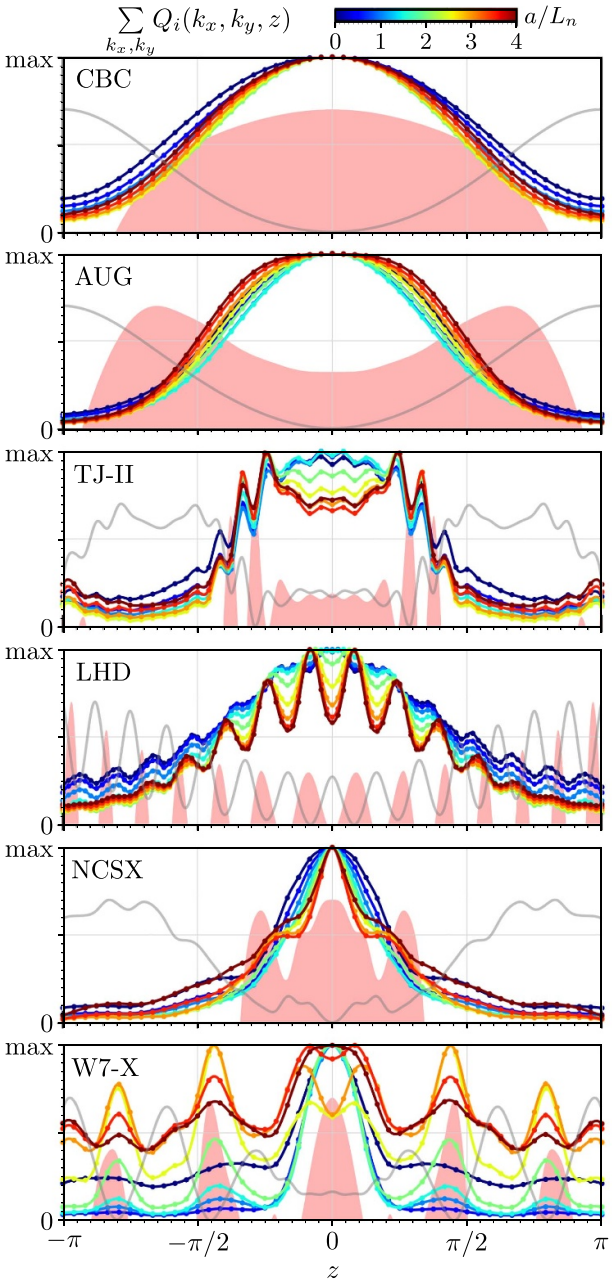


**Figure 19.** Contributions of the individual $z$-points to the ion heat flux. The strength of the magnetic field is shown in gray, regions of bad curvature for $k_x = 0.0$ in red, and the colors of the curves correspond to the $a/L_n$-scale shown on top.

losses does not change significantly when increasing the density gradient, besides the increased contribution coming from the magnetic wells. Specifically, for $a/L_n = 0.0$, the ion heat losses are the largest at the center of the field line ($z = 0$). As explained in section 4, the ITG mode, which is believed to be dominant for $a/L_n = 0.0$, drives turbulence in locations which have the most pronounced bad curvature, which typically corresponds to the center of the field line (figure 4). For CBC, AUG and NCSX the center also corresponds to the deepest magnetic well, hence the heat losses remain dominant

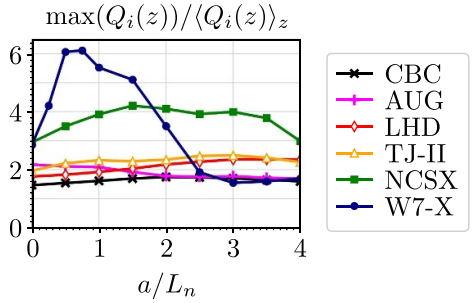


**Figure 20.** Ratio of the maximum ion heat flux along the field line with respect to the field-line averaged ion heat flux, as a function of the normalized density gradient, $a/L_n$.

at $z = 0$ as the density gradient is increased, and TEMs start playing an important role. Whereas for W7-X, LHD and TJ-II the heat losses at high density gradients predominantly arise from locations further along the field line, corresponding to the deepest magnetic wells. Moreover, for W7-X the distribution of the ion heat losses along the field line changes multiple times as the density gradient is increased. For $a/L_n = 0.0$, the heat losses arise predominately from the center of the field line, however, a substantial portion of the heat losses also arise uniformly from the entire field line. When a finite density gradient is introduced ($a/L_n = \{0.5, 1.0, 1.5\}$), the uniform contribution disappears and the heat flux is generated almost entirely at the center. For $a/L_n = 2.0$, which is close to the minimum ion heat flux (figure 16), heat losses start arising from the trapping regions, indicating that TEMs are beginning to become unstable. As the density gradient is increased further ($a/L_n = \{2.5, 3.0\}$), heat is lost inside each magnetic well, however, the heat losses in the central well are localized predominantly on the sides of the magnetic well. This could be explained by the fact that trapped electrons spend most of the time in their orbits near their bouncing points, hence the heat losses are localized here. For the highest density gradients that are considered ($a/L_n = \{3.5, 4.0\}$), the preference of the magnetic wells is diminished and instead the majority of heat losses arise uniformly from the entire field line, suggesting a significant involvement of passing electrons.

To quantify how localized the heat losses are, the maximum ion heat flux along the field line is compared to the field-line averaged heat flux in figure 20. Note that it has been demonstrated that heat losses depend on the field-line label [43], hence full-flux-surface simulations would be required to accurately discuss the localization. For CBC, AUG, TJ-II and LHD, the maximum heat flux along the field line is around twice as big as the field-line averaged heat flux, regardless of the density gradient, because the heat losses remain localized at the center of the field line. Similarly, in NCSX the localization does not change with the density gradient, however, the heat losses are much more localized. This is likely due to the fact that the bad curvature region, as well as the deepest magnetic well, are rather narrow, and the strong local magnetic shear (figure 4($c$)) damps the fluctuations arising from the two outer peaks of bad curvature. On the other hand, in

**Table 3.** Ion heat fluxes, $Q_i/Q_{gB,i}$, considering $a/L_{T_i} = 3.0$ and adiabatic electrons to isolate ion-temperature-gradient driven modes, corresponding to the blue dashed lines in figure 21.

| | $a/L_n = 0$ | $a/L_n = 1$ | $a/L_n = 2$ | $a/L_n = 3$ |
|---|---|---|---|---|
| CBC | 4.1 | 3.7 | 1.4 | 0.1 |
| AUG | 3.4 | 3.4 | 0.9 | 0.0 |
| TJ-II | 1.6 | 1.3 | 0.4 | 0.0 |
| LHD | 2.4 | 2.7 | 0.6 | 0.0 |
| NCSX | 5.8 | 4.0 | 1.0 | 0.0 |
| W7-X | 9.1 | 2.4 | 0.4 | 0.0 |

W7-X, there is a uniform loss of heat along the entire field line, as well as a strong contribution at $z = 0$ for $a/L_n = 0.0$, after which the heat losses become strongly localized to the center of the field line as the density gradient is increased. The heat losses remain strongly localized until $a/L_n = 1.5$ after which a uniform contribution along the entire field line emerges, indicating that an instability driven by passing electrons is likely becoming unstable for density gradients above $a/L_n \geqslant 2.0$.

### *6.2. Separate contributions to $Q_s$ from the ion temperature gradient and the density gradient*

To gain more insights into the trends of the heat fluxes, the contributions of the ITG-driven modes (blue dashed lines) and the density-gradient-driven modes (red dotted lines) to the ion and electron heat flux are isolated and shown in figures 21 and 22, respectively. The simulations containing both the ion temperature gradient and kinetic electrons, shown in figure 15, are represented here by the black lines. The ITG-driven modes are isolated by treating the electrons adiabatically, whereas the density-gradient-driven modes are isolated by considering vanishing temperature gradients.

The ITG-driven modes (blue dashed lines in figure 21) are stabilized with increasing density gradients, in the same way as in the linear simulations (figure 12). Under these conditions the toroidal ITG mode is believed to be dominant. Note that at $a/L_n = 0.0$ the largest ion heat flux is driven in W7-X and NCSX, and the lowest in LHD and TJ-II (see table 3). In TJ-II, including kinetic electrons in the simulations (blue lines $\rightarrow$ black lines) drastically increases the ion heat flux at $a/L_n = 0.0$, while a significant increase in the ion heat flux is observed in CBC and AUG, a moderate increase in LHD and NCSX and finally in W7-X the electron dynamics do not effect the ion heat flux at $a/L_n = 0.0$.

The ion heat flux driven by the density-gradient-driven modes (red dotted lines in figure 21) increases with increasing density gradients, which is in line with the linear results (figure 12). In this case, the turbulence is believed to be primarily driven by TEMs. At $a/L_n = 4.0$, the lowest ion heat fluxes are found in the stellarators, as shown in table 4, with NCSX having the lowest of all. As expected, the largest ion heat fluxes are found in the tokamaks, as here the majority of the trapped electrons are located in the bad curvature region. Moreover, in CBC and AUG the ion heat flux is increased significantly by the ion temperature gradient at $a/L_n = 4.0$ (red line $\rightarrow$ black line), whereas in LHD it is increased moderately. Finally, in TJ-II, NCSX and W7-X, the effect of the ion temperature gradient is very small, moreover, it is capable of reducing the ion heat flux driven by the density-gradient-driven modes.

When including both kinetic electrons and the ion temperature gradient at the same time (black lines), the ion heat flux can resemble a direct sum of the two contributions, or it is enhanced strongly. The latter is true for CBC, AUG,

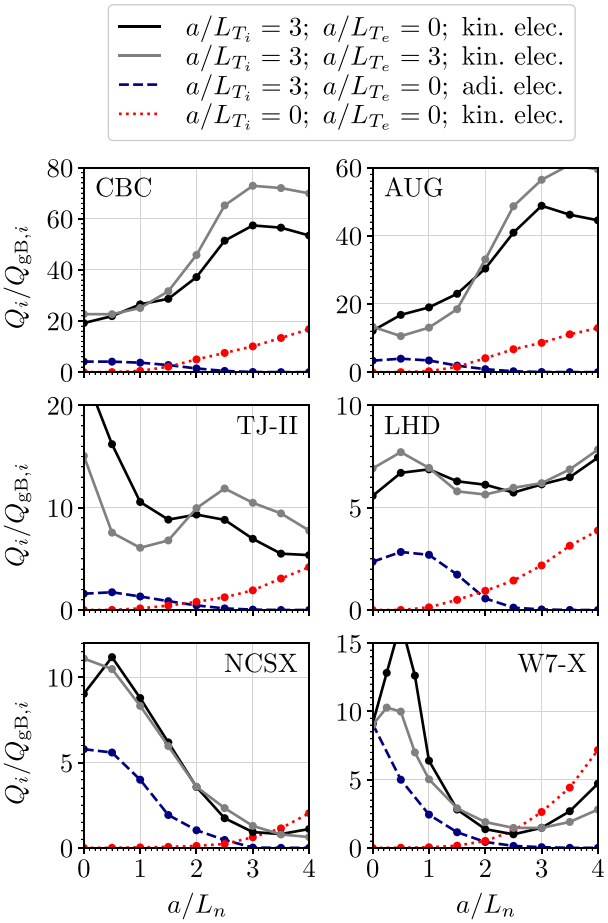


**Figure 21.** Normalized ion heat flux as a function of the normalized density gradient with kinetic electrons for $a/L_{T_e} = 0.0$ (black) and $a/L_{T_e} = 3.0$ (gray). Ion-temperature-gradient driven modes are isolated by treating the electrons as adiabatic (blue) and density-gradient-driven modes are isolated by setting $a/L_{T_i} = 0.0$ (red), both considering $a/L_{T_e} = 0.0$.

**Table 4.** Ion heat fluxes, $Q_i/Q_{gB,i}$, considering $a/L_{T_i} = 0.0$, $a/L_{T_e} = 0.0$ and kinetic electrons to isolate density-gradient-driven modes, corresponding to the red dotted lines in figure 21.

| | $a/L_n = 1$ | $a/L_n = 2$ | $a/L_n = 3$ | $a/L_n = 4$ |
|---|---|---|---|---|
| CBC | 0.5 | 5.0 | 10.1 | 16.8 |
| AUG | 0.3 | 4.1 | 8.6 | 12.9 |
| TJ-II | 0.2 | 0.8 | 1.9 | 4.2 |
| LHD | 0.1 | 0.9 | 2.2 | 3.9 |
| NCSX | 0.0 | 0.1 | 0.6 | 2.0 |
| W7-X | 0.0 | 0.5 | 2.6 | 7.2 |

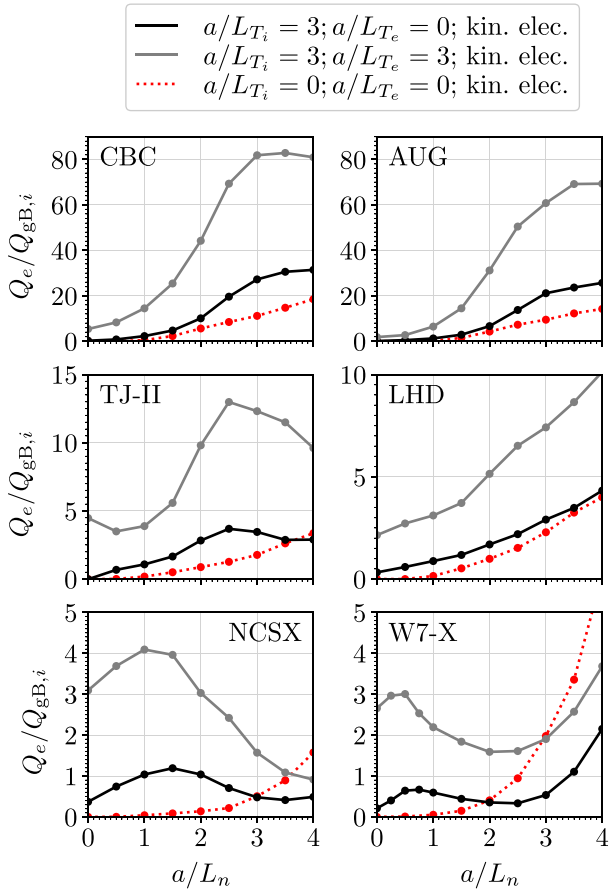


**Figure 22.** Normalized electron heat flux as a function of the normalized density gradient for $a/L_{T_e} = 0.0$ (black) and $a/L_{T_e} = 3.0$ (gray). The density-gradient-driven modes are isolated by setting $a/L_{T_i} = a/L_{T_e} = 0.0$ (red).

TJ-II and LHD, indicating that the instabilities are destabilized significantly by the free energy in the ion temperature gradient, and by the electron dynamics. In contrast, in W7-X and NCSX, the ion heat flux from the complete simulations (black lines) resembles the direct sum of the separate effects, where NCSX benefits particularly well from the weak density-gradient-driven modes (red dotted lines). Therefore, for W7-X and NCSX there is a region of density gradients for which the ITG-driven modes are being suppressed and the density-gradient-driven modes are not driving a significant amount of turbulence yet, which is qualitatively in line with the linear observations (figure 12). Moreover, from the nonlinear simulations we can conclude that the reduction of the ion heat flux by the density gradient is also related to the fact that the ITG-driven modes (blue dashed lines) in NCSX are only moderately destabilized by the electron dynamics, while they are not destabilized by kinetic electrons in W7-X, in contrast to the other devices. Additionally, the density-gradient-driven modes (red dotted lines) in NCSX and W7-X are slightly stabilized in the presence of a finite ion temperature gradient, while they are significantly destabilized in the other devices.

**Table 5.** Ion heat fluxes, $Q_i/Q_{\mathrm{gB},i}$, considering $a/L_{T_i} = 3.0$ and $a/L_{T_e} = 3.0$, corresponding to the gray curves in figure 21.

| | $a/L_n = 0$ | $a/L_n = 1$ | $a/L_n = 2$ | $a/L_n = 3$ |
|---|---|---|---|---|
| CBC | 22.7 | 25.1 | 45.8 | 72.9 |
| AUG | 13.3 | 13.1 | 33.1 | 56.4 |
| TJ-II | 15.1 | 6.1 | 10.0 | 10.5 |
| LHD | 6.9 | 6.9 | 5.6 | 6.2 |
| NCSX | 11.1 | 8.3 | 3.6 | 0.6 |
| W7-X | 9.0 | 5.0 | 1.9 | 1.5 |

**Table 6.** Electron heat fluxes, $Q_e/Q_{\mathrm{gB},i}$, for $a/L_{T_i} = 3.0$ and $a/L_{T_e} = 3.0$, corresponding to the gray curves in figure 22.

| | $a/L_n = 0$ | $a/L_n = 1$ | $a/L_n = 2$ | $a/L_n = 3$ |
|---|---|---|---|---|
| CBC | 5.4 | 14.5 | 44.2 | 81.8 |
| AUG | 1.8 | 6.4 | 31.1 | 60.8 |
| TJ-II | 4.5 | 3.9 | 9.8 | 12.3 |
| LHD | 2.1 | 3.1 | 5.1 | 7.4 |
| NCSX | 3.1 | 4.1 | 3.9 | 1.6 |
| W7-X | 2.7 | 2.2 | 1.6 | 1.9 |

### 6.3. *Effect of the electron temperature gradient*

The effect of adding a non-vanishing electron temperature gradient on the heat transport is shown in figures 21 and 22, respectively, by comparing the black lines ($a/L_{T_e} = 0.0$) with the gray lines ($a/L_{T_e} = 3.0$). The values of the ion and electron heat fluxes are summarized in tables 5 and 6, respectively. It can be seen that a finite electron temperature gradient has a relatively small effect on the ion heat losses (figure 21). Specifically, in AUG and TJ-II, the presence of an electron temperature gradient decreases the ion heat flux moderately for $a/L_n \leqslant 2.0$ and increases it for $a/L_n \geqslant 2.0$, a similar increase in the ion heat flux is observed for CBC. In W7-X, the electron temperature gradient has a moderate stabilizing effect on the ion heat loses in the presence of small density gradients, reducing the ion heat flux by 40% for $a/L_n = 0.5$.

On the other hand, the electron temperature gradient increases the drive for the electron heat transport strongly, resulting in a significant increase of the electron heat flux, which becomes of the order of the ion heat flux. Note that the electron heat flux in the absence of an electron temperature gradient (black lines in figure 22) is much smaller than the ion heat flux (black lines in figure 21), especially at low density gradients, which is expected in the presence of a steep ion temperature gradient of $a/L_{T_i} = 3.0$. Specifically, in CBC and AUG, both the electron heat flux and the ion heat flux increase with the density gradient. For LHD, the electron heat flux increases roughly linearly with the density gradient, similar as its linear growth rates. In TJ-II the electron heat flux initially decreases, after which it increases strongly with the density gradient for $a/L_{T_e} = 3.0$, comparable to the evolution of its ion heat flux. Finally, for both NCSX and W7-X, the electron heat flux undergoes a similar reduction with increasing density gradients as the ion heat flux, albeit it is less pronounced.

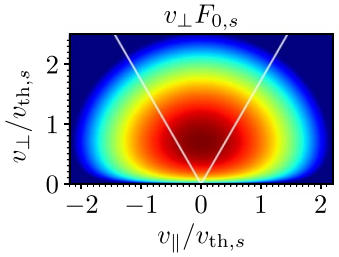


**Figure 23.** Maxwellian distribution in velocity space, with a trapping cone corresponding to $B/B_{\max} = 0.75$.

Recall that these simulations are performed at ion-Larmor scales, therefore the contribution to the heat transport that arises from the electron-Larmor scales is missing. Nonetheless, it has been shown that when the ion temperature gradient is sufficiently above the critical ion temperature gradient, the ion and electron heat flux driven at ion-Larmor scales gives an accurate picture of the heat transport in tokamaks [64, 65]. Whether or not this holds for stellarators needs to be investigated and is beyond the scope of this work.

### 6.4. Contribution of trapped and passing particles

In order to gain a better understanding of the microinstabilities that drive the turbulence, the turbulent part of the distribution function is examined in detail in this section. Let us denote by $\hat{g}_{\mathbf{k},s}$ the Fourier components of the gyro-averaged turbulent distribution function and let

$$\hat{h}_{\mathbf{k},s} = \hat{g}_{\mathbf{k},s} + \frac{Z_s e}{T_s}\,\hat{\varphi}_{\mathbf{k}}\,F_{0,s}\,J_0\left(k_\perp \rho_s\right) \tag{1}$$

be its non-adiabatic component, where $F_{0,s}$ is a Maxwellian distribution. In figure 23(*a*) Maxwellian distribution is shown as a function of the parallel and perpendicular velocities. The factor $v_\perp$ in this plot corresponds to the Jacobian of the transformation from $(v_x, v_y, v_z)$ to $(v_\perp, v_\parallel)$ velocity coordinates. Particles are trapped if $v_\parallel^2 + v_\perp^2 < 2\mu B_{\max}$, with $v_\perp^2 = 2\mu B(z)$ and $B_{\max}$ the maximum value of $B(z)$ along the field line. This trapping condition is visualized in figure 23 by the white lines—commonly known as the trapping cone. Passing particles (outside the cone) are capable of exploring the entire field line, while trapped particles (inside the cone) are confined to the magnetic wells. For a Maxwellian distribution, the fluctuations are isotropic in velocity space, and the trapped particle fraction is given by $f_{\mathrm{trapped}}(z) = \sqrt{1 - B(z)/B_{\max}}$. In figure 23, we have $f_{\mathrm{trapped}} = 0.5$, therefore, half of the particles are trapped in this scenario.

Note that a large fraction of trapped particles does not necessarily imply that trapping plays an important role on the turbulence, it may simply indicate that the magnetic well is relatively deep. Only if plots of $\hat{h}_{\mathbf{k},s}(v_\parallel, v_\perp)$ exhibit a clear deviation from isotropy, can we expect that trapping could play an important role. Moreover, $\hat{h}_{\mathbf{k},s}$ has to be sufficiently large compared to $\hat{g}_{\mathbf{k},s}$ to have a notable influence on the turbulence. Therefore, it is not sufficient to only consider the fraction of trapped particles to discuss the nature of the turbulence,

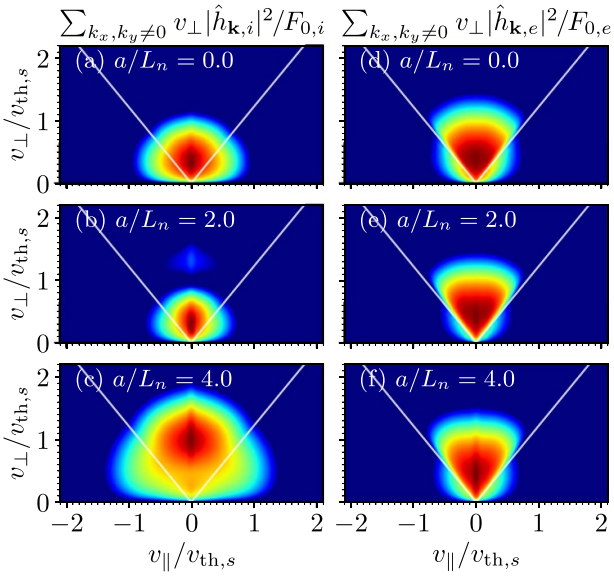


**Figure 24.** Non-adiabatic part of the distribution function at $z = 0$ for ions (left) and electrons (right) in CBC considering $a/L_{T_\mathrm{i}} = 3.0$ and $a/L_{T_\mathrm{e}} = 0.0$, for $a/L_n = 0.0$ (top row), $a/L_n = 2.0$ (middle row) and $a/L_n = 4.0$ (bottom row).

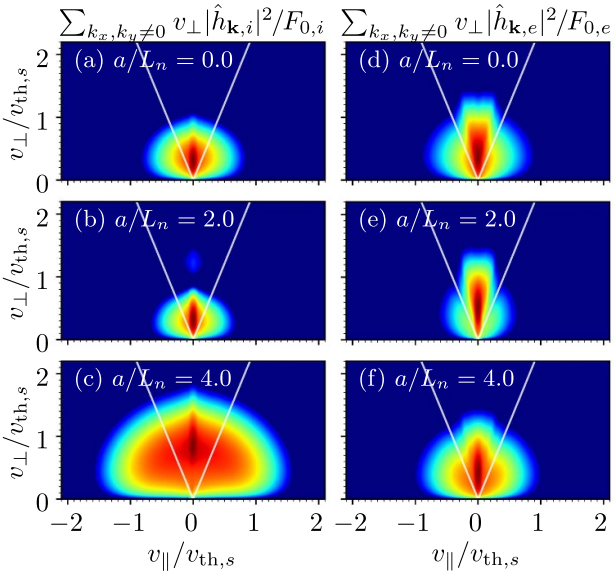


**Figure 25.** Non-adiabatic part of the distribution function at $z = 0$ for ions (left) and electrons (right) in W7-X considering $a/L_{T_\mathrm{i}} = 3.0$ and $a/L_{T_\mathrm{e}} = 0.0$, for $a/L_n = 0.0$ (top row), $a/L_n = 2.0$ (middle row) and $a/L_n = 4.0$ (bottom row).

instead, one has to carefully examine the distribution in velocity space while simultaneously taking into account the relative size of $\hat{h}_{\mathbf{k},s}$, which is discussed in the following paragraphs.

In figures 24 and 25, the non-zonal contributions to the non-adiabatic part of the distribution function for the ions and electrons, i.e. $\sum_{k_x,k_y\neq 0} |\hat{h}_{\mathbf{k},s}|^2$, are shown for CBC and W7-X at $z = 0$, considering $a/L_{T_\mathrm{i}} = 3.0$ and $a/L_{T_\mathrm{e}} = 0.0$. It is clear that for electrons trapping can play a dominant role, e.g. in CBC

the distribution function is clearly localized within the trapping region (right column of figure 24) and the electrons are strongly trapped for all density gradients. On the other hand, in W7-X the electrons are fairly trapped at $a/L_n = 0.0$, they become very trapped at $a/L_n = 2.0$ and finally they are moderately trapped at $a/L_n = 4.0$ (right column of figure 25). Note that in stellarators particles can also be trapped with respect to a local maximum of the magnetic field, which results in a more narrow trapping cone. This is observed for W7-X (right column of figure 25), which has a shallow magnetic well at the center of the field line (figure 4(*a*)). On the other hand, for CBC and W7-X, ions are more strongly trapped than in the case of an isotropic distribution (figure 23), which can be seen in the left columns of figures 24 and 25. Except for $a/L_n = 4.0$ in W7-X, where the ion distribution is almost isotropic. Note however that trapping does not necessarily play a notable role on the ion dynamics, it is possible that the instability is simply predominantly driven by ions that have small parallel velocities. This could explain why the ion distribution is rather smooth across the trapping-passing boundary, while for electrons the distribution changes strongly across the trapping-passing boundary.

To quantify the degree of non-adiabaticity and the importance of trapped particles we are going to introduce new diagnostics in the following paragraphs. Let us define

$$w(h_s,z) = \int d^3\mathbf{v} \sum_{k_x,k_y\neq 0} \frac{T_s}{2}\frac{|\hat{h}_{\mathbf{k},s}|^2}{F_{0,s}}. \tag{2}$$

Given that the role of trapped particles could be significant in $h_s$, but, at the same time, the non-adiabatic part $h_s$ could be very small compared to the distribution $g_s$ in some situations, we quantify the degree of non-adiabaticity as $w(h_\mathrm{i})/w(g_\mathrm{i})$ and $w(h_\mathrm{e})/w(g_\mathrm{e})$, which are shown in figures 26(*a*) and (*b*), respectively. Note that $w$ (with dimensions of energy density) is reminiscent to one of the pieces of the free energy (see equation (74) in [66]). This quantity is evaluated at $z = 0$ for CBC, AUG, NCSX and W7-X, and at $z = \pm 0.23$ for LHD and $z = \pm 0.54$ for TJ-II since these are the locations where the potential fluctuations peak. The parallel mode structures of the potential are not shown here, nonetheless, they are similar to the localization of the heat losses shown in figure 19, with the exception that the potential fluctuations always peak at the center for W7-X, and in the deepest wells for LHD and TJ-II, regardless of the density gradient. The parameter $z$ is henceforward dropped in $w(h_s,z)$ for simplicity.

For the ions $w(h_\mathrm{i}) > w(g_\mathrm{i})$ for all density gradients in every device (figure 26(*a*)), which means that the potential counteracts the ion dynamics. Moreover, the ratio is around unity for small density gradients, and it increases substantially at large density gradients, hence the ion dynamics are almost entirely non-adiabatic. On the other hand, for small density gradients, the contribution of the electrons is much smaller than that of the ions, i.e. $w(h_\mathrm{e}) \ll w(h_\mathrm{i})$ (figure 26(*c*)), moreover, the non-adiabatic part of the electrons is rather small, $w(h_\mathrm{e}) < w(g_\mathrm{e})$ (figure 26(*b*)). Therefore, for small density gradients, the electron dynamics do not play a significant role on the turbulence. This is expected because a vanishing

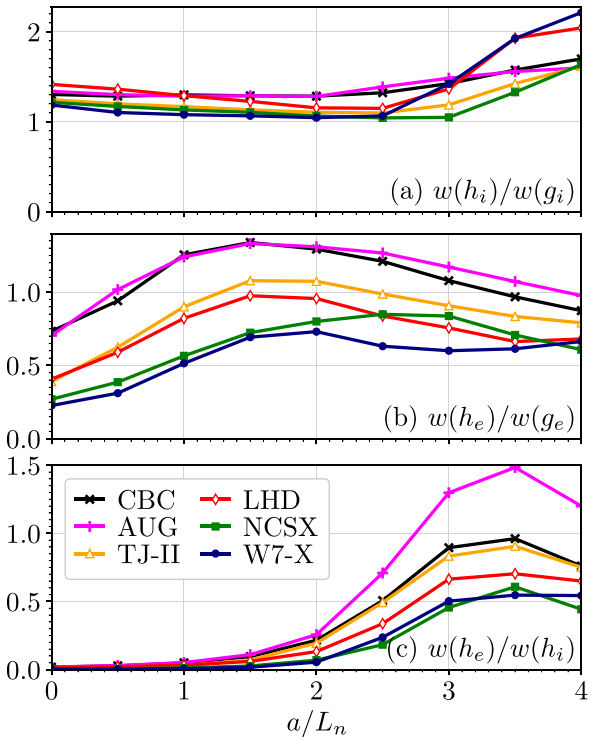


**Figure 26.** Ratio of the non-adiabatic part of the distribution function to the gyro-averaged distributed function (*a*) for ions and (*b*) for electrons, and (*c*) the fraction of the non-adiabatic part of the distribution function of the electrons to the ions, considering $a/L_{T_\mathrm{i}} = 3.0$ and $a/L_{T_\mathrm{e}} = 0.0$.

electron temperature gradient is considered here, hence when the density gradient is small, the electrons experience little to no drive, while the ions are strongly driven by the steep ion temperature gradient of $a/L_{T_\mathrm{i}} = 3.0$. As the density gradient is increased from $a/L_n = 0.0$ to $a/L_n = 1.5$, the ITG mode is damped, and while the electron dynamics remain negligible ($w(h_\mathrm{e}) \ll w(h_\mathrm{i})$), the non-adiabatic part of the electron distribution function (figure 26(*b*)) increases with the density gradient. When the density gradient is increased further, $a/L_n \geqslant 2.0$, the electron dynamics start playing an important role since $w(h_\mathrm{e})/w(h_\mathrm{i})$ becomes relatively large, reaching values around 0.5 for W7-X and NCSX, up to 1.5 in AUG (figure 26(*c*)). Moreover, the non-adiabatic part of the distribution function of the electrons is relatively large at $a/L_n = 2.0$, with $w(h_\mathrm{e}) > w(g_\mathrm{e})$ in CBC and AUG, $w(h_\mathrm{e}) \approx w(g_\mathrm{e})$ in TJ-II and LHD, while $w(h_\mathrm{e}) < w(g_\mathrm{e})$ in W7-X and NCSX. After $a/L_n = 2.0$, $w(h_\mathrm{e})/w(g_\mathrm{e})$ decreases slowly with the density gradient in CBC, AUG, TJ-II and LHD, whereas in NCSX this decrease starts after $a/L_n = 3.0$ and in W7-X the decrease starts at $a/L_n = 2.0$, however $w(h_\mathrm{e})/w(g_\mathrm{e})$ starts increasing again after $a/L_n = 3.0$.

To quantify whether the turbulence is driven by trapped or passing particles, we define a measure of the particle trapping at each point $z$ as,

$$\xi(h_s,z) = \frac{1}{w(h_s,z)} \int \mathrm{d}^3\mathbf{v}\, H_\mathrm{trap} \sum_{k_x,k_y\neq 0} \frac{T_s}{2}\frac{|\hat{h}_{\mathbf{k},s}|^2}{F_{0,s}}, \tag{3}$$

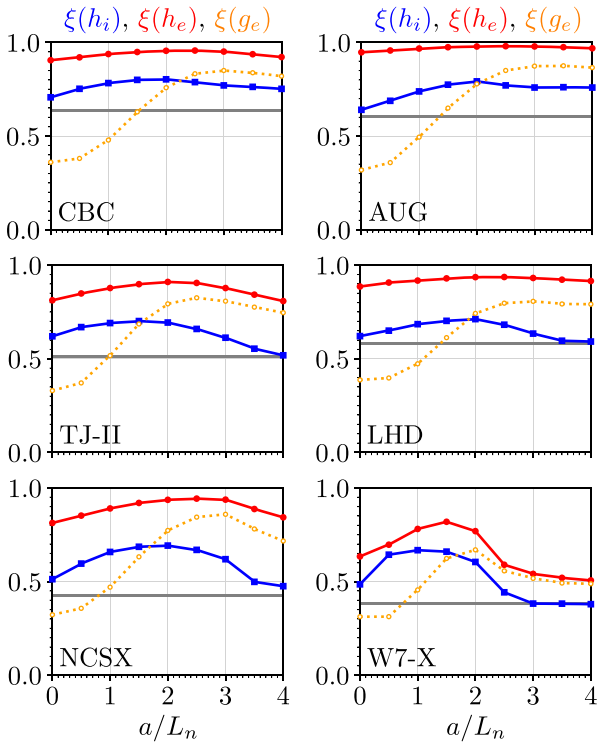


**Figure 27.** Fraction of trapped particles considering $h_\mathrm{i}$ (blue), $h_\mathrm{e}$ (red) and $g_\mathrm{e}$ (orange), for $a/L_{T_\mathrm{i}} = 3$, $a/L_{T_\mathrm{e}} = 0$, evaluated at the center of the field line ($z = 0$) for CBC, AUG, NCSX and W7-X and at $z = \pm 0.23$ for LHD and $z = \pm 0.54$ for TJ-II. The trapped particle fraction $f_\mathrm{trapped} = \sqrt{1 - B(z)/B_\mathrm{max}}$ is visualized by the horizontal gray lines.

with $H_\mathrm{trap} = H(2\mu(B_\mathrm{max} - B(z)) - v_\parallel^2)$ the Heaviside function. This measure is evaluated at the same $z$-locations considered in the previous paragraph, hence $z$ is dropped in $\xi(h_s, z)$ for simplicity. It is plotted in figure 27 considering the non-adiabatic part of the distribution function for the ions ($h_\mathrm{i}$ in blue) and the electrons ($h_\mathrm{e}$ in red), as well as for the full turbulent distribution function of the electrons ($g_\mathrm{e}$ in orange).

The quantity $\xi$ needs to be compared to the fraction of trapped particles that would occur if the fluctuations were isotropic in velocity space, which corresponds to the trapped particle fraction $f_\mathrm{trapped} = \sqrt{1 - B(z)/B_\mathrm{max}}$, represented by the gray lines in figure 27. The trapped particle fraction is 63% in CBC, 60% in AUG, 51% in TJ-II, 58% in LHD, 43% in NCSX and 38% in W7-X. For small density gradients, the majority of the ions are trapped, i.e. $\xi(h_i) > f_\mathrm{trapped}$ (blue lines in figure 27). As the density gradient is increased, $\xi(h_\mathrm{i})$ approaches $f_\mathrm{trapped}$ in the stellarators (blue lines $\rightarrow$ gray lines), because the velocity distribution becomes isotropic. In contrast, in CBC and AUG $\xi(h_\mathrm{i})$ remains high at $a/L_n = 4.0$.

On the other hand, the majority of the electrons which are driving the non-adiabatic part of the distribution function (red lines) are trapped regardless of the density gradient, i.e. $\xi(h_\mathrm{e}) > f_\mathrm{trapped}$. With the exception of W7-X, which will be discussed separately in the next section. The non-adiabatic part $h_\mathrm{e}$ contains the electrons which are driven unstable by the geometric characteristics, whereas the distribution function $g_\mathrm{e}$ also contains the contribution of the electrons that follow the perturbed electrostatic potential $\varphi$. Therefore, the geometric characteristics, such as the magnetic wells and regions of bad curvature, mostly excite trapped electrons, hence $\xi(h_\mathrm{e})$ is close to unity (red lines). Finally, looking at the full distribution function of the electrons (orange lines), it is clear that for flat density profiles the electrons are mostly passing, $\xi(g_\mathrm{e}) < f_\mathrm{trapped}$. This is because the electron dynamics do not play a notable role at small density gradients (figure 26) and hence the majority of the electrons are passing since they respond to the electrostatic potential determined by the ion dynamics. As the density gradient is increased, and the electron dynamics start playing a significant role, the majority of the electrons become trapped, $\xi(g_\mathrm{e}) > f_\mathrm{trapped}$, in CBC, AUG, TJ-II, LHD and NCSX where the TEM is believed to become dominant.

### *6.5. The case of W7-X: TEMs and passing-particle-driven universal instabilities*

The amount of trapped and passing particles that are driving the turbulence in W7-X is very different. Specifically, $\xi(h_\mathrm{e})$ is significantly lower in W7-X compared to the other five devices (red lines in figure 27), and it depends strongly on the density gradient. In particular, for small density gradients, the particles that are driving the instability become increasingly trapped as the role of the electron dynamics increases (figures 26($b$) and ($c$)), similarly as in the other devices. On the other hand, for $a/L_n \geqslant 2.5$, $\xi(h_\mathrm{e})$ decreases significantly, indicating that the turbulence is driven by both trapped and passing electrons. Therefore, in W7-X, the density-gradient-driven modes likely consist of the TEMs, as well as another instability that is driven by passing electrons, which is most likely the passing-particle-driven universal instability [55, 56]. This is supported by figure 25($f$) which shows that the non-adiabatic part of the distribution function consists of a trapped particle contribution coming from the central magnetic well (since the cone is very narrow) with the addition of an isotropic contribution which is likely originating from the passing-particle-driven universal instability. Moreover, this instability explains the large amount of heat loss across the entire field line for $a/L_n \geqslant 2.5$ in W7-X (figure 19), since passing particles explore the entire geometry. Comparing with the results in [55] this instability likely corresponds to instability (F) in the linear simulations shown in figure 9. Therefore, it is likely that in W7-X the TEM coexists with the passing-particle-driven universal instability at high density gradients. In the other five devices, the passing-particle-driven universal instability is probably absent, or subdominant to the TEM. The detailed analysis of the distribution function thus gives valuable insights into the microinstabilities which are driving the turbulence.

## 7. Conclusions

The effect of the density gradient on the turbulent heat transport is investigated by carrying out a comprehensive comparative study of different devices, including the W7-X, LHD,

TJ-II and NCSX stellarators, which represent helias, heliotron, heliac and quasi-axisymmetric configurations, respectively, as well as the AUG tokamak and the tokamak geometry of the CBC. Both linear and nonlinear simulations covering a wide range of parameters are performed, examining the effect of density gradients, as well as the presence of electrons with and without a temperature gradient. Moreover, a detailed study of the geometric characteristics—magnetic wells, curvature and shear—that drive the instabilities is conducted, and the contributions of trapped and passing particles to the turbulence are identified.

A detailed study of the linear growth rates along $(k_y\rho_\mathrm{i}, a/L_n)$ reveals that many distinct instability branches co-exist at ion-scales in W7-X, while only two branches co-exist in NCSX, which can have an important effect on the nonlinear dynamics, hence one has to be careful when studying only the most unstable mode along $k_y\rho_\mathrm{i}$. On the other hand, in the other devices a continuous transition between different microinstabilities has been observed for most of the considered density gradients, ion temperature gradients, and wavenumbers, hence the identification of the instabilities should be done very carefully or be avoided altogether. It has been shown that the growth rates increase with increasing density gradients in CBC, AUG, TJ-II, LHD and NCSX, while a moderate decrease of the growth rate is found between $a/L_n = 1.25$ and $a/L_n = 2.75$ in W7-X. Moreover, in NCSX and W7-X the growth rates of the density-gradient-driven modes exceeds those driven by the ITG-driven modes around $a/L_n \approx 2.0$, whereas this occurs around $a/L_n \approx 1.0$ for CBC, AUG, TJ-II and LHD. Therefore, in NCSX and W7-X there is a region of density gradients for which the ITG-driven modes are stabilized, without driving the density-gradient-driven modes particularly unstable yet. It is important to note that these linear studies have only taken into account the fastest-growing mode, even though subdominant modes have been shown to have a significant impact on the nonlinear state [26, 27], which is beyond the scope of this work.

The analysis is continued by performing nonlinear simulations covering a wide range of density gradients, $0.0 \leqslant a/L_n \leqslant 4.0$, considering a fixed ion temperature gradient of $a/L_{T_\mathrm{i}} = 3.0$ and taken into account both vanishing and finite electron temperature gradients. In NCSX and W7-X, a strong reduction of the ion heat flux with increasing density gradients is observed. This reduction is also evident in TJ-II for $a/L_n \leqslant 1.0$, whereas in LHD, the ion heat flux is nearly unaffected by the density gradient. In contrast, in the tokamaks, the ion heat flux increases strongly with the density gradient. Notably, the ion heat fluxes for the stellarators do not correlate with the growth rates of the fastest-growing modes obtained in the linear analysis. This indicates that underlying nonlinear saturation mechanisms, such as the nonlinear transfer of energy from unstable to damped modes [51, 58–60] and the effects of zonal flow shearing and energy cascades to dissipative scales [61–63], play a crucial role on the turbulence. Nonetheless, the strong reduction of the ion heat flux in W7-X and NCSX is partly attributed to the stabilization of the ITG-driven modes by the density gradient, without significantly destabilizing the density-gradient-driven modes. Moreover, NCSX and W7-X benefit from the fact that the ITG-driven modes are only moderately or not at all destabilized by kinetic electrons, while the density-gradient-driven modes are slightly stabilized in the presence of an ion temperature gradient. This is in contrast to the other four devices where these modes are significantly destabilized by kinetic electrons and ion temperature gradients. Furthermore, in NCSX, W7-X and TJ-II the reduction of the ion heat flux can be attributed in part to the fact that the size of the perpendicular fluctuations diminishes as the density gradient increases. Lastly, more light is shed on the nature of the microinstabilities by investigating the contributions of the trapped and passing particles to the turbulence. This reveals that TEMs are dominant at high density gradients in CBC, AUG, TJ-II, LHD and NCSX, while the passing-particle-driven universal instability drives a large part of the turbulence in W7-X.

It should be noted that the heat fluxes obtained in this paper are generally higher than those typically observed in experiments. In tokamaks, it is well established that density peaking alone cannot account for the enhanced performance of pellet-fueled discharges, and it is essential to consider additional stabilizing mechanisms, such as $E \times B$ shearing, reversed magnetic shear and high-collisionality [11–15]. In contrast, in stellarators, density peaking alone may explain the reduction in turbulence observed in devices like W7-X, NCSX, and TJ-II. This is due to the favorable properties of density-gradient-driven modes in these devices, along with enhanced nonlinear saturation mechanisms. Nonetheless, other stabilization mechanisms, such as the effects of ambipolar electric fields [20, 21] and collisions [67] are likely required to fully align with experimental observations.

## Acknowledgments

This work has been carried out within the framework of the EUROfusion Consortium, funded by the European Union via the Euratom Research and Training Programme (Grant Agreement No. 101052200—EUROfusion). Views and opinions expressed are however those of the author(s) only and do not necessarily reflect those of the European Union or the European Commission. Neither the European Union nor the European Commission can be held responsible for them. This research was supported in part by Grant PID2021-123175NB-I00, Ministerio de Ciencia e Innovación, Spain. Simulations are performed on the supercomputer Marconi (CINECA, Italy).

## Appendix A. Convergence checks

The linear and nonlinear resolutions used in this work, are given in table 7. A small amount of hyper-viscosity, with $D = 0.1$, was applied in the simulations presented in this paper. The form of the hyper-viscosity used in `stella` is given by equation (53) in [28].

**Table 7.** Resolution used for the linear and nonlinear simulations included in this paper. For nonlinear simulations, approximately 1 poloidal turn is used to ensure that $\Delta k_x = \Delta k_y$, the exact length of the flux tube is given in table 1. For LHD, $N_z = 97$ grid points are used in nonlinear simulations to account for its more detailed magnetic field structure. The Fourier grid corresponds to a computational domain of $L_x = L_y = 94\rho_\mathrm{i}$ with $N_x = N_y = 91$ grid points in real space, here $\rho_\mathrm{i}$ is the ion-Larmor radius.

| | Parallel grid | | Fourier grid | | | | Velocity grid | | | |
|---|---|---|---|---|---|---|---|---|---|---|
| | $N_\mathrm{pol}$ | $N_z$ | $k_x\rho_\mathrm{i}$ | $k_y\rho_\mathrm{i}$ | $N_{k_x}$ | $N_{k_y}$ | $v_\parallel/v_{\mathrm{th},s}$ | $v_\perp/v_{\mathrm{th},s}$ | $N_{v_\parallel}$ | $N_{v_\perp}$ |
| Linear | 3 | 513 | 0 | [0.125, 2.00] | 0 | >20 | [−3.0, 3.0] | [0.0, 3.0] | 128 | 24 |
| Nonlinear | ∼1 | 49 | [0.067, 2.00] | [0.067, 2.00] | 61 | 31 | [−3.0, 3.0] | [0.0, 3.0] | 48 | 12 |

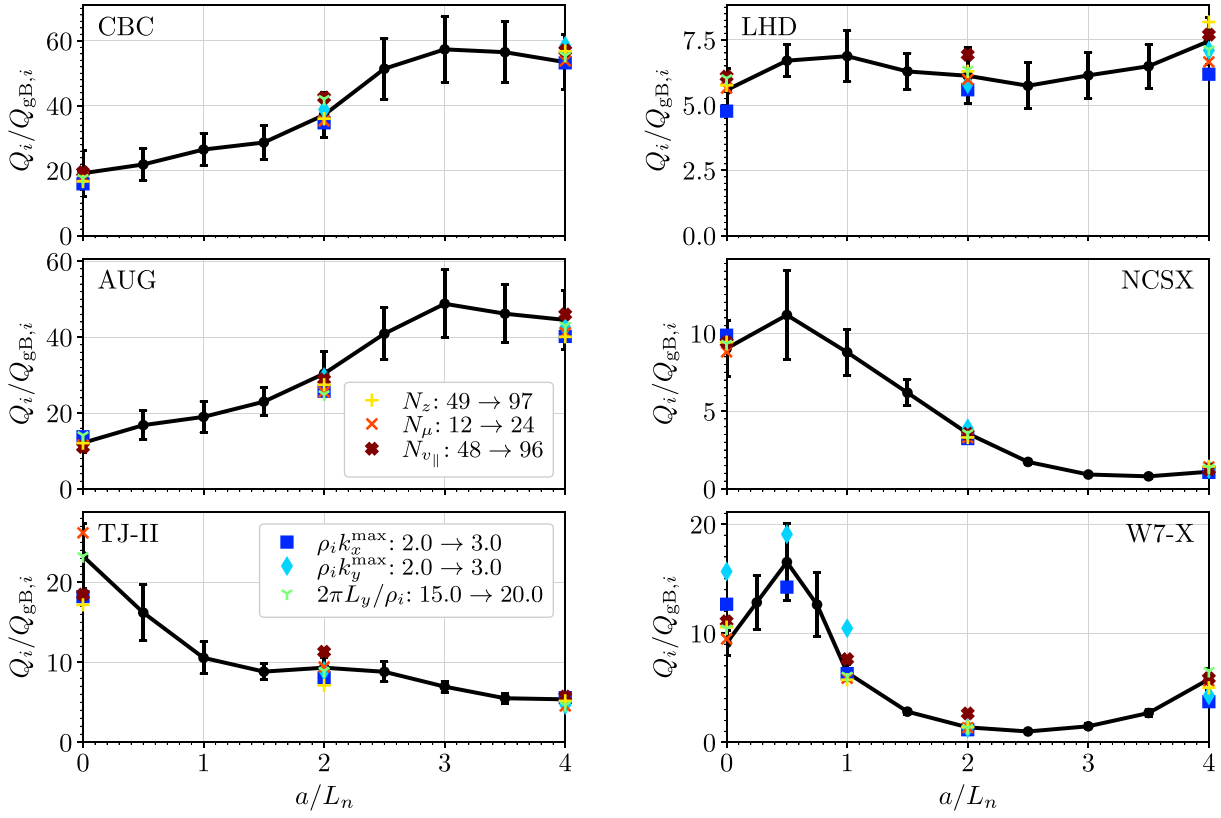


**Figure 28.** Convergence checks by increasing the nonlinear resolution parameters one by one, considering $a/L_{T_\mathrm{i}} = 3.0$ and $a/L_{T_\mathrm{e}} = 0.0$, corresponding to the simulations in figure 15. For LHD, the parallel resolution is increased from $N_z = 97$ to 193.

The nonlinear resolutions have been obtained from very rigorous convergence checks performed in W7-X for different sets of density and ion temperature gradients. The same resolution has been used for the other five devices, checking the validity of the choices by doubling the resolution parameters one by one, and examining the effect on the ion heat flux, which is shown in figure 28. Here the black lines represent the ion heat fluxes presented in figure 15. First tests for LHD revealed that $N_z = 49$ is too low in order to resolve its detailed magnetic field structure (figure 4). Therefore, a resolution of $N_z = 97$ is used for LHD and it is doubled to $N_z = 193$ in figure 28.

The error bars in figure 28 represent the standard mean deviation on the time trace of the simulation, taken between $tv_{\mathrm{th,i}}/a = 500$ and $tv_{\mathrm{th,i}}/a = 1000$, where the heat fluxes are saturated. In the simulations run with higher resolutions (colored markers), an ion heat flux has been obtained which falls within the error bars of the original simulations, hence the resolution used in this work produces reliable heat fluxes. Only in W7-X does the resolution in the perpendicular $(k_x, k_y)$-grid change the ion heat flux beyond the error bars, nonetheless, the change is not significant and it does not influence the conclusions drawn in this paper.

## Appendix B. Frequency as a function of the radial and binormal wavenumbers

In figure 7 the growth rates are shown as a function of the radial and binormal wavenumbers (section 5.1). The corresponding frequencies of these instabilities are shown in figure A1. For flat density profiles (left column) only positive frequencies are observed for all considered $(k_x, k_y)$-modes. When the density gradient is increased to $a/L_n = 2.0$ (middle column), slightly negative frequencies appear in TJ-II and W7-X around $k_x\rho_\mathrm{i} = 0.0$. Finally, negative frequencies are observed in every

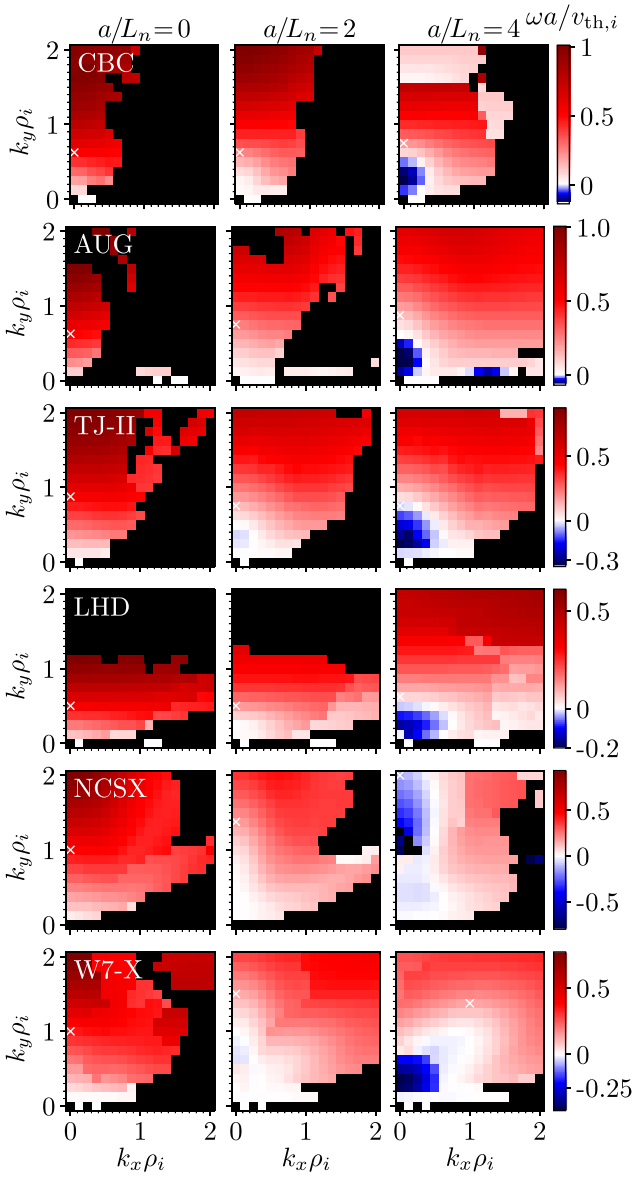


**Figure A1.** Normalized frequency as a function of $(k_x\rho_\mathrm{i}, k_y\rho_\mathrm{i})$ for $a/L_{T_\mathrm{i}} = 3.0$, $a/L_{T_\mathrm{e}} = 0.0$ and $a/L_n = 0.0$ (left column), $a/L_n = 2.0$ (middle column) and $a/L_n = 4.0$ (right column). The most unstable mode is highlighted with a white cross.

device when considering a strong density gradient of $a/L_n = 4.0$ (right column).

## Appendix C. Wavenumber of the most unstable mode as a function of the density gradient and the ion temperature gradient

In section 5.5 the growth rates and frequencies of the most unstable mode, considering $k_x = 0.0$, $k_y \leqslant 2.0$ and $a/L_{T_\mathrm{e}} = 0.0$, are shown in figures 13 and 14, respectively. The corresponding wavenumber of the most unstable mode is shown in figure B1. In NCSX and W7-X, the instabilities have smaller perpendicular scales (larger $k_y\rho_\mathrm{i}$) as the density gradient is increased. In contrast, in CBC, AUG, TJ-II and LHD, the most unstable mode retains large perpendicular scales when increasing the density gradient. Note that for W7-X, NCSX and LHD, the most unstable modes in the bottom right corners, are found at the end of our scanned range of $k_y\rho_\mathrm{i}$ values. Therefore, the growth rates and frequencies shown in figures 13 and 14 do not correspond to a peak in the $\gamma(k_y\rho_\mathrm{i})$ spectra. This is the reason why the frequency spectrum of NCSX has such negative frequencies in the bottom right corner. If one would increase the scanned $k_y\rho_\mathrm{i}$ values, the most unstable mode would be found further along the frequency branch, for higher, and possibly positive, frequencies. Nonetheless, we restricted the linear studies to $k_y\rho_\mathrm{i} \leqslant 2.0$ to remain on ion scales.

On top of each $k_y\rho_\mathrm{i}(a/L_n, a/L_{T_\mathrm{i}})$ tile, the parallel mode structure of the most unstable mode is shown, by plotting the potential squared along the field line, plotted in white if it is confined to the first poloidal turn, or in green if the

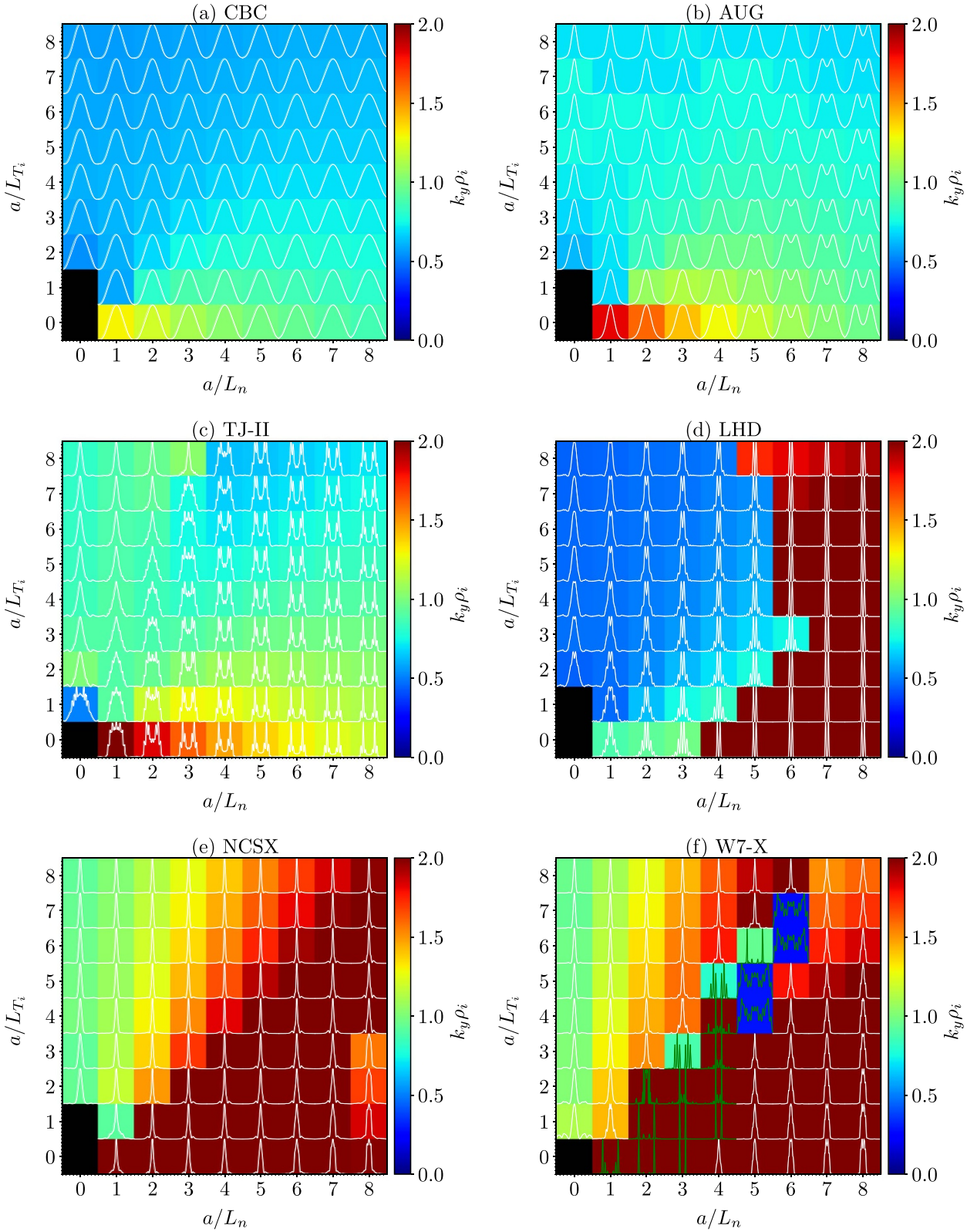


**Figure B1.** Binormal wavenumber, $k_y\rho_\mathrm{i}$, of the most unstable mode for $k_x\rho_\mathrm{i} = 0.0$ and $k_y\rho_\mathrm{i} \leqslant 2.0$, as a function of the normalized density gradient and the normalized ion temperature gradient, considering a vanishing electron temperature gradient. On top of each $k_y\rho_\mathrm{i}(a/L_n, a/L_{T_\mathrm{i}})$ tile, the parallel mode structure of the most unstable mode is shown, by plotting the potential squared along the field line, plotted in white if it is confined to the first poloidal turn, or in green if the mode extends up to three poloidal turns.

mode extends up to three poloidal turns. It can be seen that in CBC and AUG, the binormal wavenumber of the most unstable mode and its parallel mode structure change continuously throughout the scanned gradients. Similarly, in TJ-II and NCSX the binormal wavenumber and parallel mode structure change continuously for most of the scanned gradients, however, for some adjoining tiles, the mode changes rather strongly. Nonetheless by going from any tile A to tile B by first passing through other adjoining tiles, the changes are continuous. When looking at the $\gamma(k_y\rho_i)$ spectra (not shown here) this corresponds to a single peak in $\gamma(k_y\rho_i)$ which slowly splits up into two peaks as the gradients are modified. Finally, for LHD and W7-X clear jumps between distinct modes can be observed. Specifically, in W7-X, extended modes with both large and small perpendicular scales show up along $a/L_n \approx a/L_{T_i}$.

## ORCID iDs

H. Thienpondt https://orcid.org/0000-0002-0327-0853
J.M. García-Regaña https://orcid.org/0000-0001-7632-3357
I. Calvo https://orcid.org/0000-0003-3118-3463
G. Acton https://orcid.org/0000-0003-0117-6844
M. Barnes https://orcid.org/0000-0002-0177-1689

## References

[1] Sengoku S. *et al* 1985 Improvement of energy confinement time by continuous pellet fuelling in beam-heated Doublet III limiter discharges *Nucl. Fusion* **25** 1475
[2] Wolfe S.M. *et al* 1986 Effect of pellet fuelling on energy transport in ohmically heated Alcator C plasmas *Nucl. Fusion* **26** 329
[3] Milora S.L. *et al* 1986 Confinement of high-density pellet-fueled discharges in TFTR *Plasma Phys. Control. Fusion* **28** 1435
[4] Kaufmann M. *et al* 1988 Pellet injection with improved confinement in ASDEX *Nucl. Fusion* **28** 827
[5] Alladio F. *et al* 1993 MHD and confinement during pellet injection on FTU *Plasma Phys. Control. Fusion* **35** B241
[6] Tubbing B.J.D. *et al* 1991 H-mode confinement in JET with enhanced performance by pellet peaked density profiles *Nucl. Fusion* **31** 839
[7] Stroth U. *et al* 1998 High-confinement NBI discharges in the W7-AS stellarator *Plasma Phys. Control. Fusion* **40** 1551
[8] Komori A. *et al* 2006 Overview of progress in LHD experiments *Fusion Sci. Technol.* **50** 136–45
[9] Bozhenkov S.A. *et al* 2020 High-performance plasmas after pellet injections in Wendelstein 7-X *Nucl. Fusion* **60** 066011
[10] García-Cortés I. *et al* 2023 Enhanced confinement induced by pellet injection in the stellarator TJ-II *Phys. Plasmas* **30** 072506
[11] Hugon M. *et al* 1992 Shear reversal and MHD activity during pellet enhanced performance pulses in JET *Nucl. Fusion* **32** 33
[12] Smeulders P. *et al* 1995 Survey of pellet enhanced performance in JET discharges *Nucl. Fusion* **35** 225
[13] Maget P., Garbet X., Géraud A. and Joffrin E. 1999 Drift wave stability of PEP discharges in Tore Supra *Nucl. Fusion* **39** 949
[14] Baylor L.R. *et al* 2000 Improved core fueling with high field side pellet injection in the DIII-D tokamak *Phys. Plasmas* **7** 1878–85
[15] Romanelli M., Bourdelle C. and Dorland W. 2004 Effects of high density peaking and high collisionality on the stabilization of the electrostatic turbulence in the Frascati Tokamak Upgrade *Phys. Plasmas* **11** 3845–53
[16] Helander P., Proll J.H.E. and Plunk G.G. 2013 Collisionless microinstabilities in stellarators. I. Analytical theory of trapped-particle modes *Phys. Plasmas* **20** 122505
[17] Helander P., Bird T., Jenko F., Kleiber R., Plunk G.G., Proll J.H.E., Riemann J. and Xanthopoulos P. 2015 Advances in stellarator gyrokinetics *Nucl. Fusion* **55** 053030
[18] Proll J.H.E., Plunk G.G., Faber B.J., Görler T., Helander P., McKinney I.J., Pueschel M.J., Smith H.M. and Xanthopoulos P. 2022 Turbulence mitigation in maximum-J stellarators with electron-density gradient *J. Plasma Phys.* **88** 905880112
[19] García-Regaña J.M., Calvo I., Sánchez E., Thienpondt H., Velasco J.L. and Capitán J.A. 2025 Reduced electrostatic turbulence in the quasi-isodynamic stellarator configuration CIEMAT-QI4 *Nucl. Fusion* **65** 016036
[20] Xanthopoulos P. *et al* 2020 Turbulence mechanisms of enhanced performance stellarator plasmas *Phys. Rev. Lett.* **125** 075001
[21] Fu J.Y., Nicolau J.H., Liu P.F., Wei X.S., Xiao Y. and Lin Z. 2021 Global gyrokinetic simulation of neoclassical ambipolar electric field and its effects on microturbulence in W7-X stellarator *Phys. Plasmas* **28** 062309
[22] Xanthopoulos P., Mischchenko A., Helander P., Sugama H. and Watanabe T.-H. 2011 Zonal flow dynamics and control of turbulent transport in stellarators *Phys. Rev. Lett.* **107** 245002
[23] Faber B.J., Pueschel M.J., Proll J.H.E., Xanthopoulos P., Terry P.W., Hegna C.C., Weir G.M., Likin K.M. and Talmadge J.N. 2015 Gyrokinetic studies of trapped electron mode turbulence in the helically symmetric experiment stellarator *Phys. Plasmas* **22** 072305
[24] Ishizawa A., Kishimoto Y., Watanabe T.-H., Sugama H., Tanaka K., Satake S., Kobayashi S., Nagasaki K. and Nakamura Y. 2017 Multi-machine analysis of turbulent transport in helical systems via gyrokinetic simulation *Nucl. Fusion* **57** 066010
[25] Zocco A., Podavini L., Wilms F., Bañón Navarro A. and Jenko F. 2024 Electron-temperature-gradient-driven ion-scale turbulence in high-performance scenarios in Wendelstein 7-X *Phys. Rev. Res.* **6** 033099
[26] Faber B.J., Pueschel M.J., Terry P.W., Hegna C.C. and Roman J.E. 2018 Stellarator microinstabilities and turbulence at low magnetic shear *J. Plasma Phys.* **84** 905840503
[27] McKinney I.J., Pueschel M.J., Faber B.J., Hegna C.C., Talmadge J.N., Anderson D.T., Mynick H.E. and Xanthopoulos P. 2019 A comparison of turbulent transport in a quasi-helical and a quasi-axisymmetric stellarator *J. Plasma Phys.* **85** 905850503
[28] Barnes M., Parra F.I. and Landreman M. 2019 `stella`: an operator-split, implicit-explicit $\delta$f-gyrokinetic code for general magnetic field configurations *J. Comput. Phys.* **391** 365–80
[29] Dimits A.M. *et al* 2000 Comparisons and physics basis of tokamak transport models and turbulence simulations *Phys. Plasmas* **7** 969–83
[30] Rewoldt G., Ku L.-P. and Tang W.M. 2005 Comparison of microinstability properties for stellarator magnetic geometries *Phys. Plasmas* **12** 102512

[31] Proll J.H.E., Xanthopoulos P. and Helander P. 2013 Collisionless microinstabilities in stellarators. II. Numerical simulations *Phys. Plasmas* **20** 122506

[32] González-Jerez A., Xanthopoulos P., García-Regaña J.M., Calvo I., Alcusón J., Bañón Navarro A., Barnes M., Parra F.I. and Geiger J. 2022 Electrostatic gyrokinetic simulations in Wendelstein 7-X geometry: benchmark between the codes `stella` and `GENE` *J. Plasma Phys.* **88** 905880310

[33] Thienpondt H. *et al* 2023 Prevention of core particle depletion in stellarators by turbulence *Phys. Rev. Res.* **5** L022053

[34] Alonso J.A. *et al* 2024 Density profiles in stellarators: an overview of particle transport, fuelling and profile shaping studies at TJ-II *Nucl. Fusion* **64** 112018

[35] García-Regaña J.M. *et al* 2021 Turbulent impurity transport simulations in Wendelstein 7-X plasmas *J. Plasma Phys.* **87** 855870103

[36] García-Regaña J.M., Barnes M., Calvo I., González-Jerez A., Thienpondt H., Sánchez E., Parra F.I. and St.-Onge D.A. 2021 Turbulent transport of impurities in 3D devices *Nucl. Fusion* **61** 116019

[37] García-Regaña J.M., Calvo I., Parra F.I. and Thienpondt H. 2024 Reduction (or enhancement) of stellarator turbulence by impurities *Phys. Rev. Lett.* **133** 105101

[38] D'haeseleer W.D., Hitchon W.N.G., Callen J.D. and Shohet J.L. 2012 *Flux Coordinates and Magnetic Field Structure: A Guide to a Fundamental Tool of Plasma Theory* (Springer)

[39] Grimm R.C., Dewar R.L. and Manickam J. 1983 Ideal MHD stability calculations in axisymmetric toroidal coordinate systems *J. Comput. Phys.* **49** 94–117

[40] Geiger J., Beidler C.D., Feng Y., Maaßberg H., Marushchenko N.B. and Turkin Y. 2014 Physics in the magnetic configuration space of W7-X *Plasma Phys. Control. Fusion* **57** 014004

[41] Hirshman S.P. and Whitson J.C. 1983 Steepest-descent moment method for three-dimensional magnetohydrodynamic equilibria *Phys. Fluids* **26** 3553–68

[42] Miller R.L., Chu M.S., Greene J.M., Lin-Liu Y.R. and Waltz R.E. 1998 Noncircular, finite aspect ratio, local equilibrium model *Phys. Plasmas* **5** 973–8

[43] Sánchez E. *et al* 2021 Gyrokinetic simulations in stellarators using different computational domains *Nucl. Fusion* **61** 116074

[44] Dewar R.L. and Hudson S.R. 1998 Stellarator symmetry *Physica* D **112** 275–80

[45] Martin M.F., Landreman M., Xanthopoulos P., Mandell N.R. and Dorland W. 2018 The parallel boundary condition for turbulence simulations in low magnetic shear devices *Plasma Phys. Control. Fusion* **60** 095008

[46] Parisi J.F. *et al* 2020 Toroidal and slab ETG instability dominance in the linear spectrum of JET-ILW pedestals *Nucl. Fusion* **60** 126045

[47] Beer M.A., Cowley S.C. and Hammett G.W. 1995 Field-aligned coordinates for nonlinear simulations of tokamak turbulence *Phys. Plasmas* **2** 2687–700

[48] Ball J., Brunner S. and Ajay C.J. 2020 Eliminating turbulent self-interaction through the parallel boundary condition in local gyrokinetic simulations *J. Plasma Phys.* **86** 905860207

[49] Catto P.J. 1978 Linearized gyro-kinetics *Plasma Phys.* **20** 719

[50] Plunk G.G., Helander P., Xanthopoulos P. and Connor J.W. 2014 Collisionless microinstabilities in stellarators. III. The ion-temperature-gradient mode *Phys. Plasmas* **21** 032112

[51] Hatch D.R., Terry P.W., Jenko F., Merz F., Pueschel M.J., Nevins W.M. and Wang E. 2011 Role of subdominant stable modes in plasma microturbulence *Phys. Plasmas* **18** 055706

[52] Kammerer M., Merz F. and Jenko F. 2008 Exceptional points in linear gyrokinetics *Phys. Plasmas* **15** 052102

[53] Pueschel M.J., Faber B.J., Citrin J., Hegna C.C., Terry P.W. and Hatch D.R. 2016 Stellarator turbulence: subdominant eigenmodes and quasilinear modeling *Phys. Rev. Lett.* **116** 085001

[54] Plunk G.G., Connor J.W. and Helander P. 2017 Collisionless microinstabilities in stellarators. Part 4. The ion-driven trapped-electron mode *J. Plasma Phys.* **83** 715830404

[55] Costello P., Proll J.H.E., Plunk G.G., Pueschel M.J. and Alcusón J.A. 2023 The universal instability in optimised stellarators *J. Plasma Phys.* **89** 905890402

[56] Podavini L., Zocco A., García-Regaña J.M., Barnes M., Parra F.I., Mishchenko A. and Helander P. 2024 Ion-temperature-and density-gradient-driven instabilities and turbulence in Wendelstein 7-X close to the stability threshold *J. Plasma Phys.* **90** 905900414

[57] Alcusón J.A., Xanthopoulos P., Plunk G.G., Helander P., Wilms F., Turkin Y., von Stechow A. and Grulke O. 2020 Suppression of electrostatic micro-instabilities in maximum-J stellarators *Plasma Phys. Control. Fusion* **62** 035005

[58] Terry P.W., Baver D.A. and Gupta S. 2006 Role of stable eigenmodes in saturated local plasma turbulence *Phys. Plasmas* **13** 022307

[59] Hegna C.C., Terry P.W. and Faber B.J. 2018 Theory of ITG turbulent saturation in stellarators: identifying mechanisms to reduce turbulent transport *Phys. Plasmas* **25** 022511

[60] Terry P.W., Faber B.J., Hegna C.C., Mirnov V.V., Pueschel M.J. and Whelan G.G. 2018 Saturation scalings of toroidal ion temperature gradient turbulence *Phys. Plasmas* **25** 012308

[61] Terry P.W. 2000 Suppression of turbulence and transport by sheared flow *Rev. Mod. Phys.* **72** 109

[62] Diamond P.H., Itoh S.-I., Itoh K. and Hahm T.S. 2005 Zonal flows in plasma—a review *Plasma Phys. Control. Fusion* **47** R35

[63] Plunk G.G., Banón Navarro A. and Jenko F. 2015 Understanding nonlinear saturation in zonal-flow-dominated ion temperature gradient turbulence *Plasma Phys. Control. Fusion* **57** 045005

[64] Howard N.T., Holland C., White A.E., Greenwald M., Candy J. and Creely A.J. 2016 Multi-scale gyrokinetic simulations: comparison with experiment and implications for predicting turbulence and transport *Phys. Plasmas* **23** 056109

[65] Howard N.T., Holland C., White A.E., Greenwald M. and Candy J. 2015 Multi-scale gyrokinetic simulation of tokamak plasmas: enhanced heat loss due to cross-scale coupling of plasma turbulence *Nucl. Fusion* **56** 014004

[66] Schekochihin A.A., Cowley S.C., Dorland W., Hammett G.W., Howes G.G., Quataert E. and Tatsuno T. 2009 Astrophysical gyrokinetics: kinetic and fluid turbulent cascades in magnetized weakly collisional plasmas *Astrophys. J. Suppl. Ser.* **182** 310

[67] Kauffmann K. 2012 Including collisions in gyrokinetic tokamak and stellarator simulations *PhD Thesis* Ernst-Moritz-Arndt-Universität Greifswald